PHOTONIC DEVICES UTILIZING SUBWAVELENGTH LIGHT CONFINEMENT

by

Yi-Hao Chen

A dissertation submitted in partial fulfillment
of the requirements for the degree of
Doctor of Philosophy
(Electrical Engineering)
in The University of Michigan
2011

Doctoral Committee:

Associate Professor Jay Guo, Chair
Professor Herbert Graves Winful
Associate Professor Xudong Fan
Assistant Professor PC Ku

Dedicated to my parents, my wife, and my daughter for their love and support

ACKNOWLEDGEMENTS

It is my great pleasure to acknowledge many people who made this possible. First of all, I would like to mention my deepest gratitude to my advisor Professor L. Jay Guo who has been a great mentor providing support and guidance throughout my PhD study. He has been very considerate in many aspects of both our research and my life. He has helped me to overcome many difficulties and problems with his patience, encouragement, and understanding of my circumstances. The completion of my research projects and degree would have been impossible without his assistance.

I would like to thank Professor PC Ku, Professor Herbert Graves Winful, Professor Xudong Fan, and Professor Rachel S Goldman for their time and effort to participate in my thesis proposal, to evaluate my dissertation, and to participate in my oral defense. Special thanks are given to Professor PC Ku, who has provided me many helpful advices throughout out my study and in the nanolaser project. I must also acknowledge the support from many collaborators. The work in the nanolaser project would not be done without Professor Pallab Bhattacharya, Yi-Kuei Wu, Min Kim, Chi-Sen Lee, Wei Guo, and Jeremy Moore. Professor Fred Terry, Alex Kaplan, and Brandon Lucas have provided generous help to the work in the metamaterials and the plasmonic sensing.

I am honored to work with other talented members in nanogroup: Professor Dawen Li, Dr. Li-Jing Cheng, Dr. Myung-Gyu Kang, Dr. Se-Hyun Ahn, Dr. Phillip Choi, Dr. Pran Mukherjee, Dr. Carlos Pina, Hyoun Won Baac, Sung-Liang Chen, Hyunsoo Kim,

Jae Yong Lee, Tao Ling, Hui Joon Park, Ting Xu, and Dr. Haofei Shi. I am also blessed to have good friends in Ann Arbor: Hsun-Yi Chen, Richard Hou, Hsien-Kai Hsiao, Hing-Fang Hsieh, Sean Huang, Kuo-Ken Huang, Chi-Shan Li, Kai-Hsiu Liao, Tsai-Wei Wu, and many others.

Last but not least, I want to express the greatest gratitude to my father, Wu-Hsiung Chen, my mother Ching-Hui Tang, my sister Yi-Hsiang Chen, and particularly my wife Meng-Hwa Lin for their love and support to myself and my beloved daughter, Mia Chen.

TABLE OF CONTENTS

LIST OF FIGURES

ABSTRACT

Photonic devices utilizing subwavelength light confinement have been of interest due to many interesting optical properties introduced by the peculiar field distributions in the structures of subwavelength feature sizes. As a result of recent advances in nanofabrication, these photonic devices can now be experimentally demonstrated. We present our theoretical and experimental studies of several subwavelength structures showing the optical responses different from other structures.

First, we investigated the optical properties of deep subwavelength metallic structures with finding their magnetic and electric resonances. These magnetic and electric resonances can lead to electromagnetic properties not existing in nature. We designed a new split-ring resonator (SRR) geometry which has negative permeability and negative permittivity in order to construct low loss negative index materials. The new design helped to make the operating wavelength shifted down to visible region from the infrared region where most of other SRR geometries operate. Next, because of the field enhancements arising from the electric resonances, metallic nanoparticles had been previously studied for sensing using the amplitude response of the electronic resonances. However, the phase response could also carry important information. We investigated both the amplitude and phase responses of anisotropic and uniformly oriented gold nanoparticles and the relation between them.

Additionally, we studied the guidance of light utilizing the surface modes. Surface modes supported at metal surface propagates with a larger effective index, a larger

confinement factor, and a smaller mode size than modes in an air-cladded waveguide. We proposed metal-capped microdisk cavities supporting surface modes in the transverse dimension. Having a larger effective index reduces the radiation loss and can increase the cavity Q factor. Having a larger cavity Q factor, a larger confinement factor, and a smaller mode size can lower the threshold for lasing. However, these benefits are accompanied by the additional propagation loss of surface modes introduced by the metal absorption. To reduce this metal absorption, we designed alternative structures which incorporate metal-sandwiched and photonic crystal structures in the transverse dimension. By improving the performances of subwavelength cavities, they can serve as the substantial building blocks for integrated optics.

Chapter 1

Introduction

1

1.1 Background

Subwavelength optics opens many new phenomena and potential applications and has drawn plenty of attention in recent years due to the advances in the techniques for fabricating nanoscale structures[1-8]. At a scale shorter than the wavelength of light, the interactions between light and matter no longer follow the macroscopic conventions. The optical responses depend not only on the properties of the bulk materials but also on the size and the shape of the subwavelength structures. The strong light-matter interactions generate unique optical field distributions which are directly related to the topography of photonic nanostructures. There light-matter interactions could the lead to field localization in subwavelength volumes and give rise to the distinctive optical responses to the light excitation.

1.2 Interaction of Light with Matters

The interactions of light with matters follow Maxwell's equations. For subwavelength structures, these interactions depend on both the electromagnetic properties of the materials the topography of the structures. The electromagnetic properties of materials can be characterized by the permittivity and the permeability

describing the responses to electric field and the magnetic field respectively. For materials in nature, the response to magnetic field of visible light are weak and can only produce small deviations of permeability from the value in free space. However, artificial materials can have the strong response to magnetic field of visible light and the effective permeability can deviate more from the permeability of free space[9]. Artificial materials with the strong response to magnetic field can enable new optical properties and exciting applications. One of the most interesting properties is a negative refractive index which will be explored in more details in Chapter 2. On the other hand, the response to the electric field can be characterized by the permittivity and is usually much stronger than the response to magnetic field. Different response to the electric field leads to different conductivity. Conductivity is linearly proportional to the imaginary part of permittivity. Materials are commonly classified into metals, semiconductors, and dielectrics according to their conductivity which again is directly related to the response to electric field.

To understand the microscopic picture of the interaction between light and matters, atoms or molecules of the media of interest are commonly treated as harmonic oscillators by Lorentz Model. The response of harmonic oscillators to light can be characterized by complex-valued permittivity through Lorentz Model. The complex-valued permittivity governed by macroscopic Maxwell's equations can thus be linked to the microscopic interactions between light and atoms or molecules. Meanwhile, as a result of causality, the real and imaginary parts of permittivity are not independent and can be related through Kramers-Kronig relations. These relations will be utilized in Chapter 3 to relate the real and imaginary parts of transmission coefficients. When excited by light, atoms or molecules of the medium can radiate energy as they behave like harmonic oscillators.

The process of radiation by particles of size much smaller than the wavelength of light is referred as Rayleigh scattering[10-12]. The strength of Rayleigh scattering varies with the size but not the shape of particles. When the size of particles is similar to the wavelength, the scattering of light by the particles is referred as Mie scattering. While the strength of the scattering depend highly on both the size and the shape of particles, it does not vary with the wavelength of light if the material is transparent (not absorbing). Furthermore, the scattering becomes dispersive when the material is absorbing and the process is referred as resonant scattering[13]. When the absorbing material is metal, the scattering resonance is referred as the localized surface plasmon resonance (LSPR)[8]. The properties of localized surface plasmon resonance with metallic nanoparticles will be discussed in the next section and in Chapter 3..

If light is scattered by periodic structures with the lattice constant comparable to the scale of wavelength, the interference of scattered light is referred as diffraction[14]. Such structures with the periodic arrangement of objects at a length scale comparable to light are commonly referred as the photonic crystals[15, 16]. The interference of scattered or diffracted light can lead to the control over light propagation by prohibiting the propagation of certain electromagnetic waves. This control of light propagation may provide good confinement of light or photons. Photonic crystals are the optical analog of semiconductor crystals which can confine electrons by periodic arrangement of atoms or molecules at the length scale of de Broglie wavelength of electrons. Although there are no crystals in nature with lattice constants comparable to the wavelength of light, artificial structures can be fabricated with desired lattice constants. Optical cavities

utilizing the light confinement provided by photonic crystal will be discussed in Chapter 5.

1.3 Metal Optics

It has been found that one of the most efficient ways to channel and concentrate light below the diffraction limit is to use metals because its negative permittivity[1, 4, 17-20]. Electromagnetic waves are evanescent in media like metals having negative permittivity. Because light cannot propagate in metals, metals can serve as good reflectors and are used to guide and confine light. [21]. On the other hand, when the excitation of electric field is polarized perpendicular to the metal surface (TM), light can interact with the free electrons of metals coherently. In the process of this interaction, the free electrons respond collectively by oscillating in resonance with the electromagnetic field as illustrated in Figure 1.1 (a). The resonant interactions between the surface charge oscillation and the electromagnetic field of the light constitute the so called surface plasmon polaritons (SPPs)[1]. SPPs can be guided at the interface between a metal and a dielectric medium of SPP waveguides.

SPPs have two unique properties. First, the fields exponentially decay with normal distance from the interface as depicted in Figure 1.1 (b). The field localization to the surface of metal makes the size of SPP modes generally smaller than the modes in dielectric waveguides. Reducing the cavity mode volume by utilizing a SPP waveguide to provide the transverse confinement for whispering gallery modes (WGMs) will be discussed in Chapter 4. Second, the momentum of a SPP mode is larger than that of a free pace photon in the dielectric medium. The dispersion relation for a SPP mode is given by

Equation (1.1) where k_{SPP} and k_0 denote the wavevector of a SPP mode and a free space photon and ε_m and ε_d denote the permittivity for the metal and the dielectric medium. It can be clearly seen from Equation (1.1) that when ε_m and ε_d have opposite signs k_{SPP} is always larger than k_0 as plotted in Figure 1.1 (c). In Chapter 4., we will discuss how this larger momentum can help to reduce the radiation loss of WGM and increase the cavity Q factor. However, because of the nonzero conductivity of metals which contribute to the nonzero imaginary part ε_m, k_{SPP} contains imaginary part which leads to the propagation loss for a SPP mode. This propagation loss arises from metal absorption and need to be added into the total loss for a SPP guided WGM. In Chapter 4, we will discuss the reduction this propagation loss by incorporating WGM with a long range surface plasmon polariton (LRSPP) mode. In most cases, a smallest propagation loss is preferred. For all metallic structures in this dissertation, we use silver or gold since they have the lowest absorption among all metals.

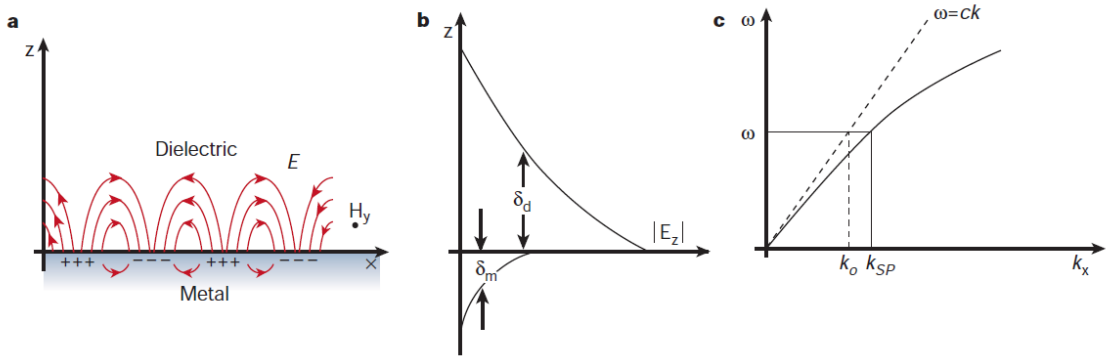

Figure 1.1(a) SPPs at the interface between a metal and a dielectric material have a combined electromagnetic wave and surface charge character. They are transverse magnetic (H is in the y direction), and the generation of surface charge requires an electric field normal to the surface. (b) Electric field component perpendicular to the surface being enhanced near the surface and decaying exponentially with distance away from it. δ_d is the decay length in the dielectric medium above the metal and is on the order of half of the

wavelength. δ_m is the decay length into the metal determined by the skin depth and is usually one order smaller than the wavelength. (c) The dispersion curve for a SPP mode shows the SPP mode always has greater momentum (k_{SP}) than a free space photon (k_0) of the same frequency ω. [1]

$$k_{SPP} = k_0 \sqrt{\frac{\varepsilon_d \varepsilon_m}{\varepsilon_d + \varepsilon_m}} \tag{1.1}$$

When light interacts with metallic particles of size smaller than the wavelength of light, the electrons oscillate locally around the nanoparticle with a frequency known as the LSPR. As mentioned in the previous section, strong resonant scattering occurs when the wavelength of light is at the LSPR[22] The interaction between the electron cloud of the metallic particles and the electromagnetic fields of light is illustrated in Figure 1.2. A LSPR is characterized with a strong extinction band and an enhancement of the local electromagnetic fields. The extinction band is the result of the resonant scattering and the metal absorption. It not only depends on the electromagnetic properties of the metal and the surrounding dielectric material, but also depends on the size and shape of the metallic particles. These dependencies can be seen in Equation (1.2) which calculates the extinction spectrum of the simplest structure, a metallic sphere. Here, ε_m and ε_d denote the permittivity of the metal and the surrounding dielectric material while a denotes the radius of the metallic sphere. Because of the field enhancements near the metallic nanoparticles, the change in the extinction spectrum with the surrounding dielectric material can be applied to sensing which will be discussed in Chapter 3.

$$E(\lambda) = \frac{24\pi^2 N a^3 \varepsilon_d^{\frac{3}{2}}}{\lambda ln(10)} \left[\frac{Im[\varepsilon_m(\lambda)]}{(Re[\varepsilon_m(\lambda)] + 2\varepsilon_d)^2 + Im[\varepsilon_m(\lambda)]^2} \right] \quad (1.2)$$

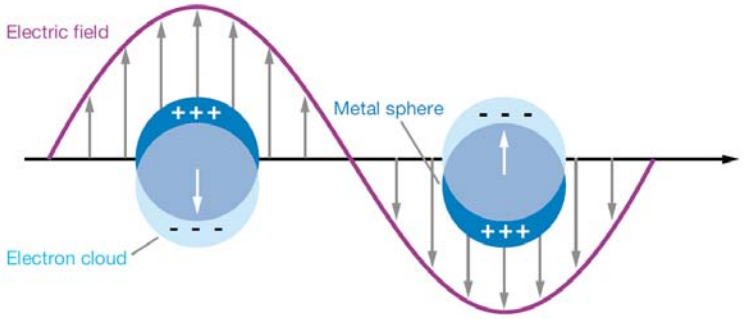

Figure 1.2A schematic diagram illustrating a localized surface Plasmon[8].

1.4 Numerical Analysis

Although the interaction between light and maters completely follows Maxwell's equations, the analytical solutions of some complicated structures are difficult or sometimes impossible to find. For example, the analytical solution for the extinction spectrum of metallic nanoparticles can be found only for sphere and spheroid[8], for all other shapes of nanoparticles, additional approximations need to be applied when searching for appropriate solutions[23, 24]. Therefore, in order to study the optical properties of more complicated subwavelength structures, we usually rely on numerical simulations. One of the most commonly used numerical simulation methods in dealing with the electromagnetic waves is the finite difference time domain (FDTD) method[25]. The FDTD algorithm has been widely used to study LSPR[26-31], SPP waveguide[32-34], and microcavities[35-42]. The development of the FDTD method can be traced back to the introduction of Yee's grid in 1966[43]. FDTD method is a space-grid time-domain

technique and can obtain rigorous solutions to Maxell's curl equations. It can solve for any electromagnetic field components at any sampled points of space and time within the simulation domain. It can simulate the actual propagation of electromagnetic waves by marching in time in a time-stepping scheme. The distribution of fields (Chapter 2), transmission and reflection coefficients (Chapter 2), scattering of particles (Chapter 3), absorption due to the dielectric properties of metals (Chapter 2, Chapter 3, and Chapter 4), and radiation from optical cavities (Chapter 4 and Chapter 5) can all be simulated using the FDTD method. Moreover, the dispersive optical properties can also be obtained by doing frequency analysis from a pulse response with FDTD simulations. The basics of the FDTD method will be discussed in more details in Appendix.

1.5 Chapter Overview

In this dissertation, several interesting subwavelength geometries consisting of dielectric and metallic materials were presented. Their attractive optical properties and potential applications were investigated by characterizing their magnetic, plasmonic, and cavity resonances. The macroscopic properties of some deep-subwavelength structures can be described by homogeneous media with effective electromagnetic responses. In search of negative refraction, metamaterials based on split-ring resonators were studied. Negative permeability introduced by the magnetic resonances along with negative permittivity introduced by metal was demonstrated at visible wavelengths in Chapter 2. The field localizations at the plasmonic resonances of metallic nanoparticles may result in field enhancements applicable to sensing. The polarization dependent plasmonic resonances of anisotropic nanoparticles were exploited with spectroscopic ellipsometry

and an effective sensing configuration was explored in Chapter 3. The field localizations in subwavelength volumes could be help to shrink the size of microcavities reducing the cavity mode volumes. Metal coating was used to support surface modes and to increase the field confinement in the transverse dimension of microdisk cavities. Metallic microdisks with cavity Q factors higher than that in traditional microdisks were presented with subwavelength microdisk diameters in Chapter 4. Another type of surface modes with lossless propagation supported by truncated photonic crystal was also incorporated with the design of microdisk cavities. With the help from reducing the mode volumes, increasing the cavity Q factors, and reducing the threshold gain, the lasing of microcavities was demonstrated in Chapter 5.

Chapter 2

Magnetic Response of Connected Split Ring Resonators at Visible Frequencies

2

2.1 Introduction

As introduced in Chapter 1, some electromagnetic properties not possessed by materials in nature can be demonstrated by artificial structures. When the artificial structures are periodic, the individual responses from the features of each unit can usually constitute a single response for the entire periodic structure. Two types of periodic structures of particular interest to researchers in recent years are photonic crystals and metamaterials. Photonic crystals (PCs) are usually dielectric periodic structures of lattice constants comparable to the wavelength[15, 44]. The responses of PCs can be described well by the photonic band gaps in their dispersion diagram. We will leave the details of PCs in Chapter 5 when we discuss the light confinement with PCs in microcavities. On the other hand, if the lattice constants are small enough such that the periodic structures can be treated as homogeneous media, they are in the metamaterial regime. The upper limit of lattice constants of metamaterials is a quarter of wavelength (effective-homogeneity limit)[45]. This limit ensures that the scattering or diffraction which is prominent in PC regime is much less important in this metametrial regime. Below this limit, electromagnetic waves only probe the averaged response from the entire periodic

structures with well defined constitutive permittivity ε and permeability μ. Since these artificial structures do not exist in nature, the effective ε and μ characterizing metamaterials can be very different from the ε and μ of materials in nature.

Several types of metamaterials and applications have been proposed in recent years including: chiral materials[46, 47], nonlinear optics[48, 49], super resolution[50], metamaterial absorber[51], and cloaking[52, 53], One of the most extensively studied topics is negative-index metamaterials. The idea of negative-refraction was first introduced by Veselago in 1968[54]. He concluded that when the ε and μ of a medium are simultaneously negative, the direction of phase velocity (determined by the wavevector) is opposite to the direction of power flow (determined by the Poynting vector). It was proved later that this requirement for negative refraction can be somewhat released with a condition given by Equation (2.1) , where ε_r and μ_r are the real part of ε and μ[55]. The effectiveness of negative refraction is represented by the figure of merit (FOM) for negative-index metamaterials given by Equation (2.2) , where n_r and n_i(loss) are the real and imaginary part of refractive index n. Although the condition of simultaneously negative ε_r and μ_r is not necessary, this condition is still desired for achieving high FOM (low loss).

$$\varepsilon_r|\mu| + \mu_r|\varepsilon|_r < 0 \tag{2.1}$$

$$FOM = \frac{|n_r|}{n_i} = \frac{|\varepsilon_r|\mu| + \mu_r|\varepsilon|_r|}{\varepsilon_i|\mu| + \mu_i|\varepsilon|_r} \tag{2.2}$$

While there are materials with negative ε such as metals, there are no materials in nature possessing negative μ at optical frequencies because of the weak interaction of atoms with magnetic field component. The investigation of negative refraction had not

drawn much attention before Pendry proposed the idea of using split-ting resonators (SRRs) to mimic magnetism to give negative μ at high frequencies in 1999[56]. Furthermore, Later in 2000, he also predicted that “perfect lens” can be constructed with negative index metamaterials to achieve resolution beyond the diffraction limit[57]. Since then, the negative index matamaterials have become of one of the hottest topics and (SRRs) have been extensively studied as negative permeability metamaterials[58-60].

In this chapter, we study the properties of SRR structure. Based on theoretical understanding and numerical simulations, we design new SRR structures in the goal of achieving negative refractive index at visible wavelengths. Since the proposed structures can be asymmetric along the propagation direction, we also present the derivation an index retrieval method for structures with asymmetric responses to electromagnetic waves in the propagation direction. We show experimental results that confirm our theoretical perdition of negative refractive index at visible wavelengths.

2.2 Characteristics of SRRs

SRRs are consisting of metallic loops or rings with small gaps. Their magnetic resonances can be excited by magnetic field component normal to the plane of the metallic rings to generate electromagnetic responses similar to the LC resonators. At their magnetic resonances, circulating currents are generated around the metallic loops and those currents in turn generate induced magnetic fields to oppose the incident magnetic fields based on Lenz’s Law. The induced magnetic fields could tailor the effective μ of SRRs. The magnetic resonance wavelength determined by resonance of the LC circuit is inversely proportional to the square root of the product of inductance and capacitance[61]. Because the values of both the effective inductance and capacitance of SRRs depend on

their size, the magnetic resonance wavelength scales proportionally with the size of SRRs in the microwave regime when metals acts as ideal conductors. However, when the wavelength approaches the metal plasma oscillation wavelength, metals can no longer be treated as ideal conductors. The metal plasma oscillation wavelength normally resides in the visible or ultraviolet regime. The size scaling of SRRs with resonance wavelength usually breaks down below infrared wavelengths. Therefore, the wavelength of magnetic resonance of SRRs giving negative permeability has an lower limit at 800nm[62, 63]. Several variations of SRRs have been proposed to push the magnetic resonance wavelengths to visible regime [61, 62, 64, 65]. As mentioned previously, in order to achieve negative refractive index with low loss, it is desired to have simultaneously negative ε_r and μ_r. The SRRs mentioned in above references show negative μ_r only. Although it has been proposed that placing metal wire along with SRRs can achieve negative permeability and permittivity simultaneously [66], the combination of metal wires with SRRs in 3D structure is extremely difficult in fabrication. To resolve the difficulties, we proposed a standing connected SRR structure that can give negative ε_r and μ_r simultaneously at visible wavelengths without incorporating metal wire.

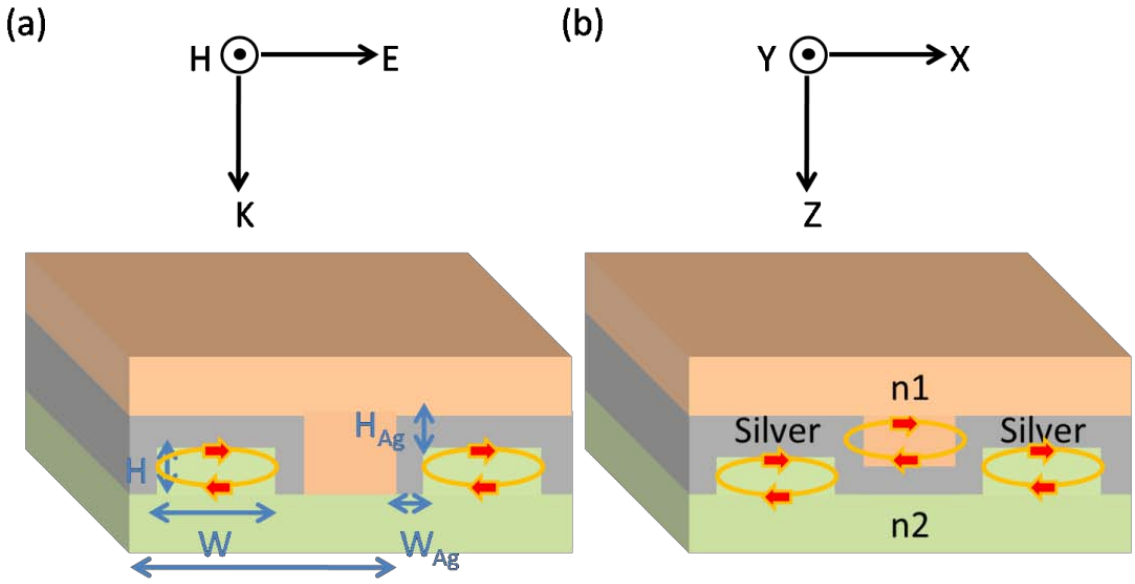

Figure 2.1(a) Disconnected and (b) connected SRRs. The light polarization shown is TM with magnetic field H in the transverse (y) direction.

First, the magnetic resonance need to be excited with magnetic field component normal to the plane of rings, oblique incidence was needed in other structures when the SRRs lie on sample surface. Our standing SRRs could relieve this requirement because there always can be a magnetic field component normal to the plane of our standing rings regardless of the incident angle. In other SRR structures, SRRs are usually disconnected. As opposed to disconnected SRRs shown in Figure 2.1(a), the structure shown in Figure 2.1(b) is formed by connected SRRs. The continuous metal layer provides negative ε_r over a broad range of wavelengths similar to that of flat metal film. The introduction of a parallel capacitance reduces the total capacitance and increase the LC frequency which is inversely proportional to the resonance wavelength. The magnetic resonance and thus negative μ_r can be achieved at visible wavelengths. We will later discuss the optimization of the connected SRRs based on numerical analysis.

2.3 Index Retrieval

The effective permeability and permittivity can be retrieved from complex transmission and reflection coefficients as described in Reference[67]. However, for structure possessing asymmetry along the propagation direction, the transmission and reflection coefficients are also expected to be different from forward and backward propagation directions. The effective ε and μ can be asymmetric as well. While a modified retrieval method has been discussed to address this issue[68], this retrieval method only applies to unit cell that is periodic in the propagation direction. Here we derived a simpler set of equations to solve for the effective electromagnetic properties of any asymmetric structure

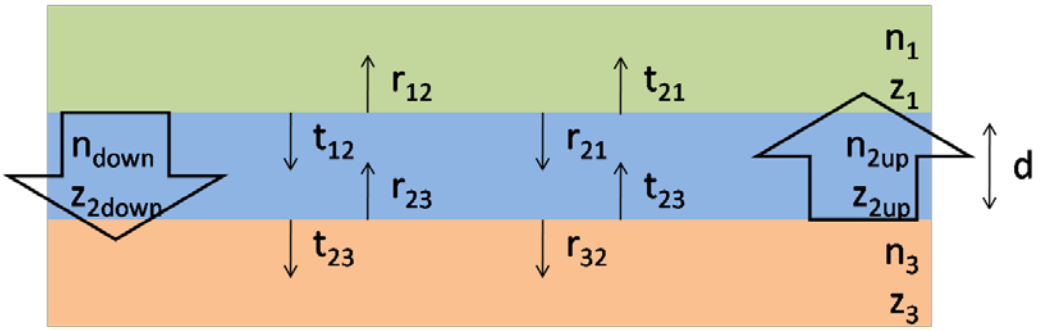

Figure 2.2Transmission and reflection coefficients associated with a three-layer system. The thickness of layer 2 is d. Refractive index and impedance are dependent of propagation direction in layer 2 but are independent of propagation direction in layer 1 and 3. t_{mn} represents the transmission coefficient from layer m to n while r_{mn} represents the reflection coefficient from layer n to m.

To accurately retrieve the effective material parameters, we consider a three-layer system depicted in Figure 2.2. With known refractive index and impedance in layer 1 and 3, we want to solve for the asymmetric refractive index and impedance from measurable transmission and reflection coefficients. Measurable transmission and reflection

coefficients are given by Equation (2.3) and Equation (2.4) for downward propagation and Equation (2.5) and Equation (2.6) for upward propagation.

$$t_{down} = \frac{t_{12}\exp(in_{2down}\,kd)t_{23}}{1 - r_{23}\exp(in_{2up}\,kd)\,r_{21}\exp(in_{2down}\,kd)} \tag{2.3}$$

$$r_{down} = r_{12} + t_{down}\,\frac{r_{23}t_{21}}{t_{23}}\exp(in_{2up}\,kd) \tag{2.4}$$

$$t_{up} = \frac{t_{32}\exp(in_{2up}\,kd)t_{21}}{1 - r_{23}\exp(in_{2up}\,kd)\,r_{21}\exp(in_{2down}\,kd)} \tag{2.5}$$

$$r_{up} = r_{32} + t_{up}\,\frac{r_{21}t_{23}}{t_{21}}\exp(in_{2down}\,kd) \tag{2.6}$$

Equation (2.3) to (2.6) can be rearranged into Equation (2.7) to (2.10)

$$t_{up}\,t_{down} - (r_{down} - r_{12})\left(r_{up} - r_{32} + t_{32}\frac{t_{21}}{r_{23}}\right) = 0 \tag{2.7}$$

$$\exp(in_{2up}\,kd) = \frac{(r_{down} - r_{12})t_{23}}{t_{down}\,r_{23}\,t_{21}} \tag{2.8}$$

$$t_{up}\,t_{down} - (r_{up} - r_{32})\left(r_{down} - r_{12} + t_{12}\frac{t_{21}}{r_{21}}\right) = 0 \tag{2.9}$$

$$\exp(in_{2down}\,kd) = \frac{(r_{up} - r_{32})t_{21}}{t_{up}\,r_{21}\,t_{23}} \tag{2.10}$$

The transmission and reflection coefficients t_{12}, t_{21}, t_{23}, t_{32}, r_{12}, r_{21}, r_{23}, and r_{32} can be represented in terms of z_1, z_{2up}, z_{2down}, and z_3. Therefore, z_{2up} and z_{2down} can be solved from Eq. (2.7) and (2.9) n_{2up} and n_{2down} can be solved from Equation (2.8) and (2.10) with known z_{2up} and z_{2down}. The effective μ and ε can be calculated from refractive index and impedance by μ=nz and ε=n/z. Thus, for any medium imbedded in other media of known ε and μ, material parameters which are either symmetric or asymmetric can be retrieved by this method.

2.4 Numerical Analysis

In order to retrieve the effective ε and μ using Eq. (2.7) to (2.10) we used the finite-difference-time domain (FDTD) method described in Appendix The Finite-Difference-Time-Domain Method to obtain the complex transmission and reflection coefficients for both downward and upward propagation. We applied dispersive refractive index of silver in the simulations. Grid size is set as 1 nm considering the penetration depth in silver is about 10 nm at visible wavelengths. Periodic boundary conditions were used to obtain the response of the entire periodic structures by simulating with only unit cell. The excitation source is set as plane wave with a pulsed temporal function for frequency analysis. The dispersive complex transmission and reflection coefficients could be calculated from the monitored temporal transmission and reflection functions using Fourier analysis.

With simulated transmission and reflection coefficients, the effective ε and μ can be retrieved using Equation (2.7) to (2.10) The results are shown in Figure 2.3. Because both structures are asymmetric along the propagation direction, the effective ε and μ are different for light propagating upward and downward. At the magnetic resonance, the induced magnetic field can either be in the same or different direction of the external filed. The direction and strength of induced magnetic field can affect the effective permeability [56]. For disconnected SRRs, the induced magnetic field only exists inside the rings as seen from the field profile illustrated in Figure 2.4(a). For connected SRRs, the induced field exists both inside and in between the rings seen from the field profile illustrated in Figure 2.4(b). The stronger induced field results in the stronger response to magnetic field for connected SRRs compared to that for disconnected SRRs. Therefore,

while the real μ_r always stays positive for disconnected SRRs, negative μ_r can be achieved at around 825nm for connected SRRs in downward propagation. On the other hand, the electric resonance of disconnected SRRs is stronger than that of connected SRRs. Unlike disconnected SRRs, the electric response of connected SRRs is similar to that of a flat metal film. Negative ε_r can be achieved over a large bandwidth for connected SRRs above the electric resonance wavelength which is at about 800nm shown in Figure 2.3 (d). It is interesting to see that ε_r and μ_r is of opposite sign if the propagation direction is opposite. Because of the mismatch between the polarity of ε_r and μ_r, negative ε_r and μ_r can't be simultaneously achieved with the same propagation direction in this configuration.

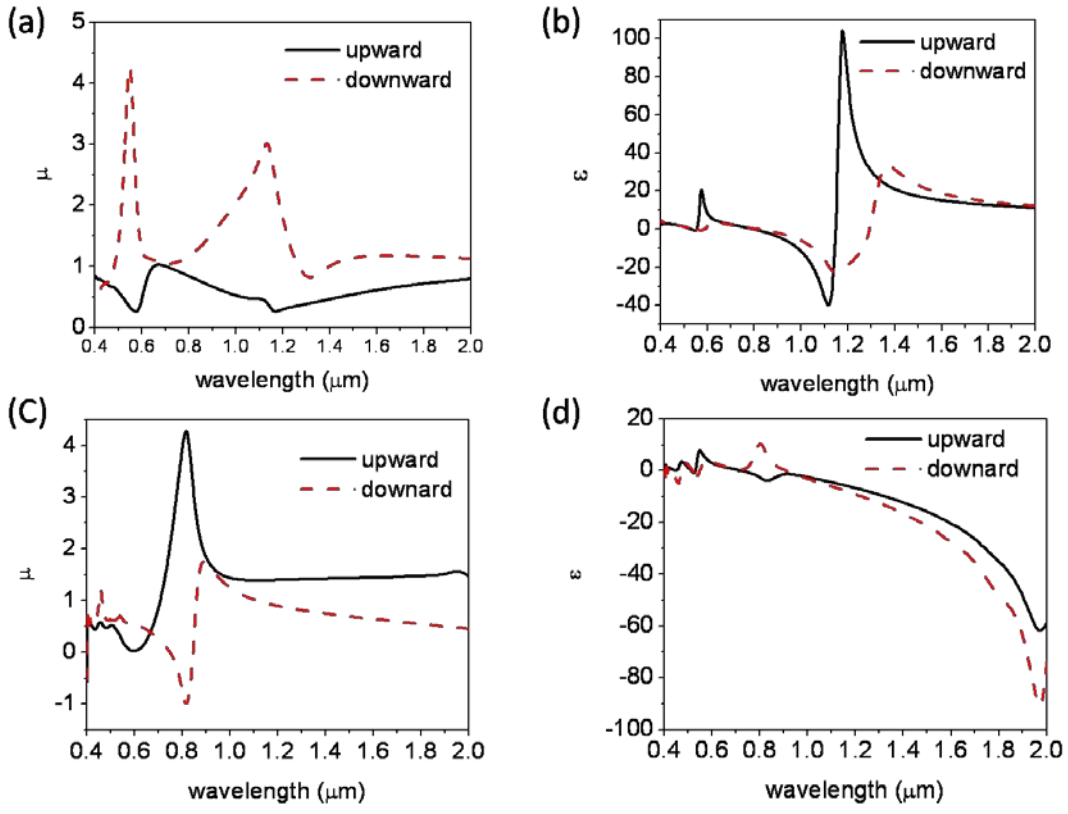

Figure 2.3(a) Retrieved real part of μ and (b) ε of disconnected SRRs depicted in Figure 2.1 (a). (c) Retrieved real part of μ and (d) ε of connected SRRs depicted in

Figure 2.1(b). For both structures, n1 = 1, n2 = 1.55, Period = 220nm, W = 100nm, H = 50nm, and H_{Ag} = W_{Ag}=10nm. Black solid and red dashed curves are retrieved from upward and downward propagation respectively.

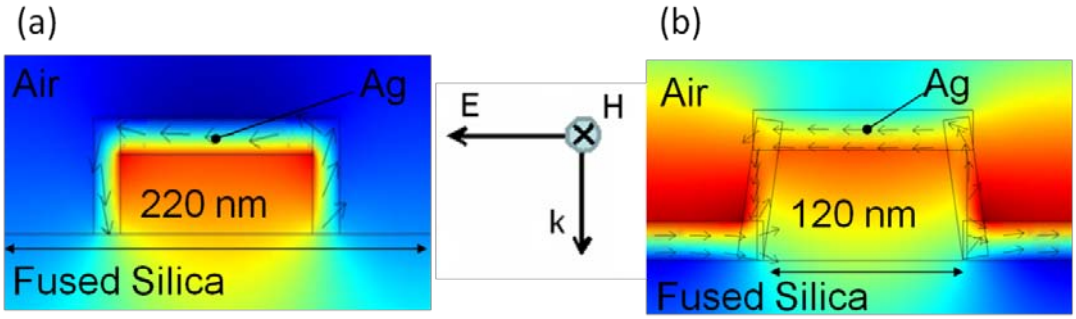

Figure 2.4COMSOL simulations from Reference [69] for the (a) disconnected SRRs at the magnetic resonance wavelength (800 nm) and (b) connected SRRs at the magnetic resonance wavelength (570nm) showing the normal component of the magnetic field. The direction (normalized magnitude) of the electric displacement is shown with arrows.

We tried to adjust several structure parameters of connected SRR in the goal of optimizing the electromagnetic response for realizing negative refractive index material. We found that simultaneous negative ε_r and μ_r can be achieved by adding a coating layer matching the index of substrate as shown in Figure 2.5.

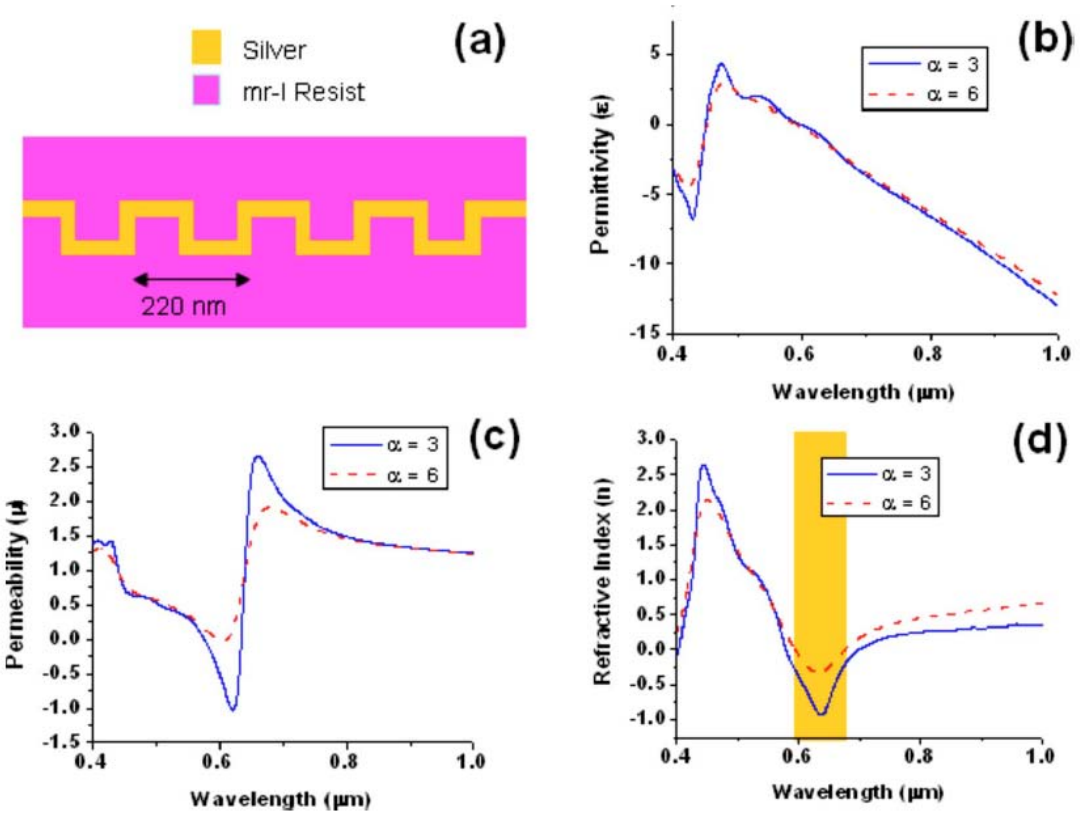

Figure 2.5(a) Diagram of the ideal symmetric connected SRRs made from 25 nm of Ag sandwiched by mr-I layers. Simulated (b) ε_r (c) μ_r and (d) n_r with different damping factor α (associated with damping coefficient in Appendix The Finite-Difference-Time-Domain Method) accounting for the variation in ε of the metal formed with different conditions[69].

2.5 Experimental Results

To demonstrate the real sample of proposed structure, the structure is fabricated with nanoimprint lithography with procedures similar to Reference [69]. Spin-coated mr-I resist on silica substrate was imprinted with a SiO_2 grating mold with a period of 220 nm, depth of 50 nm and roughly 50% duty cycle by thermal nanoimprint lithography. A conformal silver coating of about 20 nm was deposited on imprinted mr-I. Another mr-I layer was coated on top of silver layer to match the index of the substrate. An SEM image of fabricated SRRs is shown in Figure 2.6.

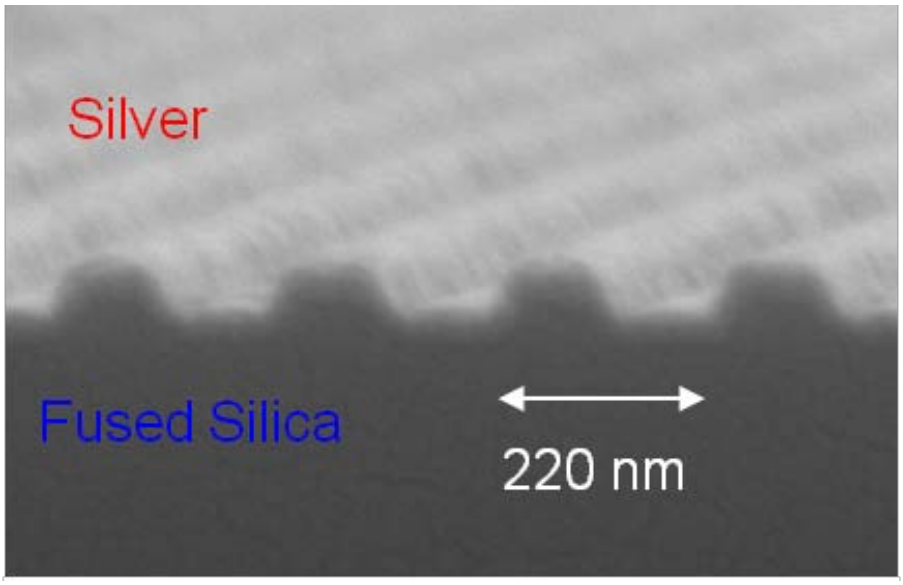

Figure 2.6SEM image from Ref. 13 of continuous SRRs without top mr-I coating.

Ellipsometry spectra were measured with a Woollam variable angle spectroscopic ellipsometer WVASE32. tan(Ψ) and Δ represents the amplitude ratio and the phase difference between TE and TM transmission or reflection coefficients. The experimental curves of Ψ and Δ are given in Figure 2.7 (a) and (b). The simulated Ψ and Δ can be matched to the experimental results by adjusting the structure parameters and damping factor used in simulation. The small deviations between experiment and simulation may arise from the imperfections in fabrications such as inhomogeneous surface roughness or the deviation of permittivity of silver from bulk values near electric and magnetic resonances[70]. As both the amplitude and phase responses from experiment agree with simulation the simulation results, the retrieved electromagnetic parameters from simulation can be considered valid to describe the real sample. More accurate structure parameters than those measured from SEM image can also be obtained while searching for the match between simulation and experiment if the material properties are known. The height of structure is 15 nm smaller than the imprinting mold. The silver coating on

the sidewall is 5 nm thinner than the top and bottom because of the nonuniformity introduced by the directional silver deposition. The retrieved n shown in Figure 2.7 (c) shows that negative refractive index can be achieved around 590nm where retrieved ε_r and μ_r are simultaneously negative as shown in Figure 2.7 (d).

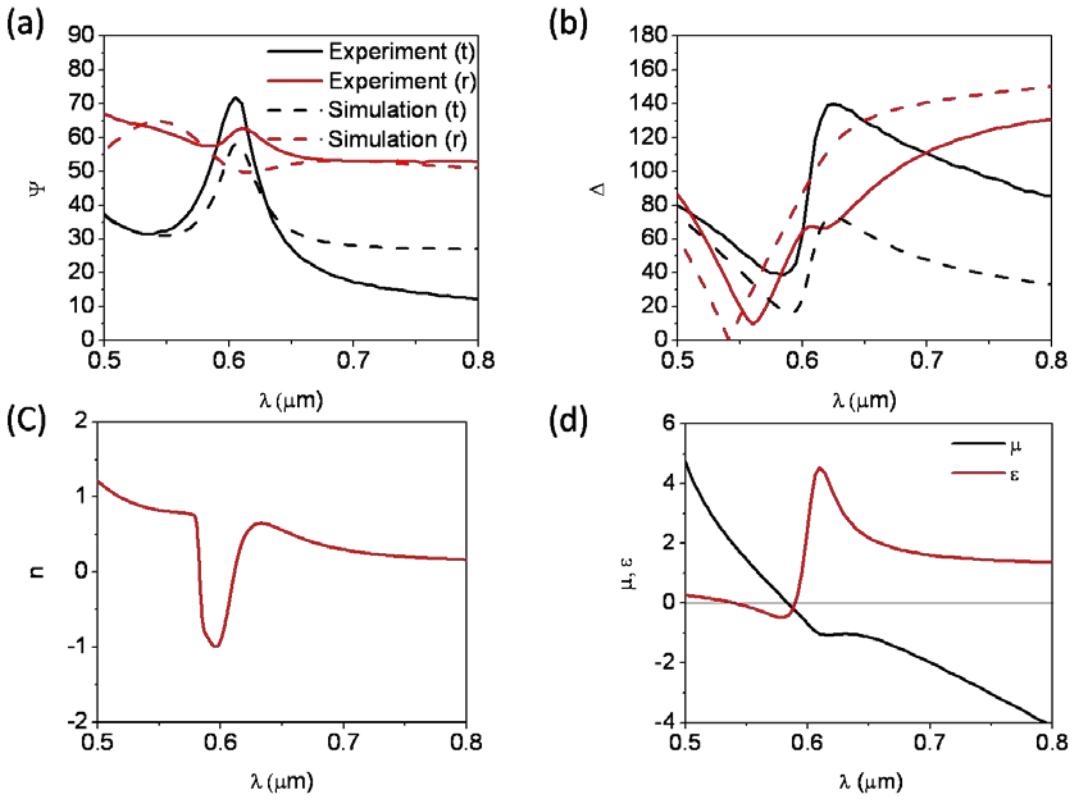

Figure 2.7Experimental and simulated (a) Ψ and (b) Δ. Retrieved (a) n and (b) μ and ε from simulated transmission and reflection coefficients. n1 = n2 = 1.45, Period=220nm, W=80nm, H=35nm, and H_{Ag}=20nm W_{Ag}=15nm. Black and red curves in (a) and (b) are from transmission and reflection ellipsometry respectively.

2.6 Conclusion

In this chapter, we have studied the magnetic resonances of a type of periodic metallic nanostructures most commonly used for constructing negative index materials. With the help of FDTD simulations and our index retrieval method, we have analyzed

and optimized the electromagnetic responses of SRRs for negative refraction. With the help of nanoimprint and ellipsometry, we experimentally proved our prediction that connected SRRs can achieve negative index of refraction at 590nm. To the best of our knowledge, this structure demonstrates negative refraction with the shortest wavelength up to date. Last but not least, I would like to especially thank Alex Kaplan for his contributions to make this work complete.

.

Chapter 3

Ellipsometrically Probed Plasmonic Resonances in Arrays of Anisotropic Gold Nanoparticles

3

3.1 Introduction

In Chapter 1, we discussed the characteristic of Localized surface Plasmon resonance (LSPR) which is a result of the collective electron density oscillations in metallic nanostructures. Excitation of LSPR by light results in local field enhancements and enhanced scattering and absorption of light. The resonant wavelength of LSPR depends on the size, shape, dielectric environment, and the type of material of the nanostructures[22]. LSPR can find applications in near-field microscopy[71], extraordinary light transmission[72], Plasmon waveguide[73], and many others. The most common widely investigated application of LSPR is sensing. There are two primary mechanisms for sensors utilizing LSPR. One is surface-enhanced Raman scattering (SERS) sensing which is based on amplified signal provided by the field enhancements. [74]The other is wavelength-shifting sensing which is based on the dependency of LSPR on its surrounding dielectric environment[75]. While both surface plasmon resonance (SPR) and LSPR has been exploited for sensor applications[8, 76]. However, sensors based on SPR require additional coupling mechanisms for light to be coupled from free space to the SPR modes. Phase detection has been shown to provide much higher

sensitivity than amplitude detection in SPR sensing[77-80]. However, LSPR sensing so far has been limited to extinction amplitude detection [81]. The phase associated with the light transmission through nanoparticles (NPs), which could carry useful information about the media, have largely been neglected partly due to the inability to create uniform and oriented NP arrays. A uniform array of anisotropic NPs has a LSPR wavelength that should depend on the polarization state of the excitation light[82]. The change of amplitude and phase of light passing through nanostructures should also depend on the polarization of excitation light.

Here, we first present the polarization dependent LSPRs of anisotropic NP arrays with experiments and simulations. Because spectroscopic ellipsometry (SE) provides ample information for metrology based on the polarization dependent optical properties of structured media[83], SE is used to study the amplitude and phase relationship of the polarization dependent LSPR. We associate the response in phase with amplitude using Kramers-Kronig relations and establish a model which could interpret the both the phase and amplitude information of any polarization dependent systems.

3.2 Experimental and Numerical Results

While Metallic NPs can be fabricated by using chemical synthesis it is difficult to immobilize them on a substrate for sensor applications and is difficult to obtain uniform distribution and spacing[84]. Similar to Chapter 2, the fabrication technique used to precisely control the size, shape and spacing of the NPs was based on nanoimprint lithography (NIL)[85, 86]. The nanoimprinting was performed by using a nanostructure mold followed by metal deposition and a lift-off process. Large area NP arrays with different shape as well as different distribution can be fabricated using this approach.

Figure 3.1 shows the SEM pictures of two examples of the NIL molds as well as the arrays of metallic NPs fabricated by using this technique. The large area NIL molds were made by successive imprints of two gratings. The mold patterns can be controlled by the orientation of the gratings and thus can give accurate control of the shape and alignment of metallic NPs. Details of the fabrication process can be found in Reference [87]. It is the perfect alignment of these large area nanostructures that leads to the polarization dependency of LSPR.

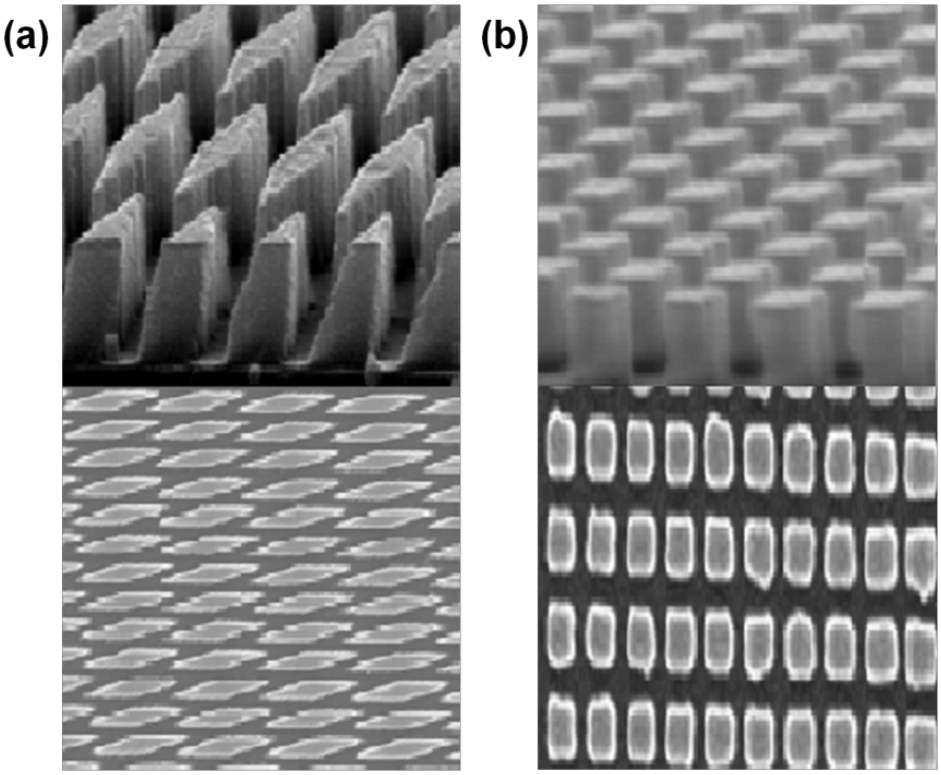

Figure 3.1SEM images of representative NIL molds (top) and imprinted metallic NP arrays (bottom) of (a) diamond and (b) rectangular shape. For the rectangular NP array, the in-plane dimensions of NPs are 115 nm and 128 nm and the lattice constant is 200 nm.

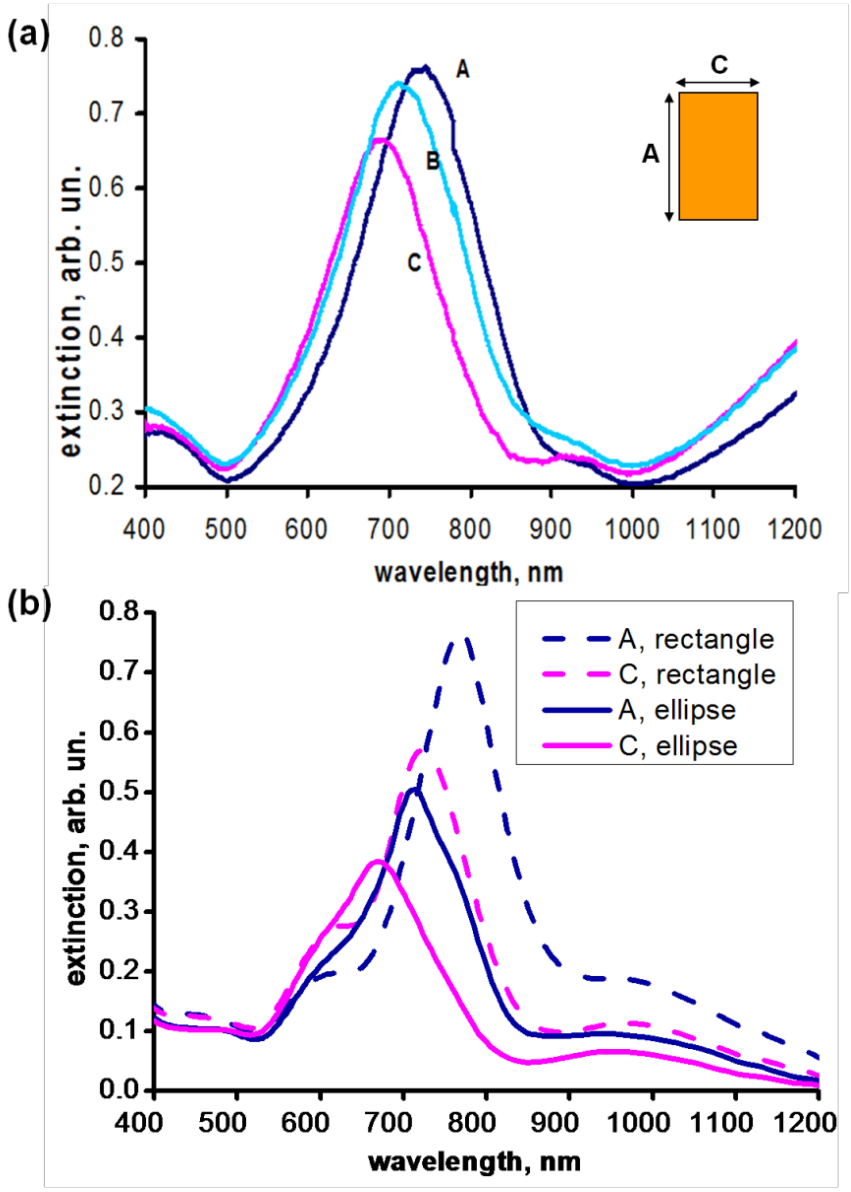

Figure 3.2(a) Measured extinction spectrum of a rectangular gold NP array and (b) simulated extinction spectrum of both a rectangular (dashed) and elliptic (solid) gold NP array where spectrum A is measured for excitation light polarized along the longer axis of the rectangular NPs, spectrum C for the shorter axis, and spectrum B is for unpolarized light.

The gold NPs with rectangular shape as shown in Figure 3.1 (b) has in-plane dimensions of 115 nm and 128 nm. The slight anisotropy of the structure leads to the dependence of LSPR on the polarization state of the excitation light and presents itself as

a suitable candidate for SE study. Light polarized along the longer in-plane axis of the rectangular NPs is expected to excite LSPR at longer resonant wavelengths and vice versa. Our measured extinction spectrum shown in Figure 3.2 (a) corroborates this statement.

We used the finite-difference-time domain (FDTD) method described in Appendix

The Finite-Difference-Time-Domain Method to obtain the extinction spectrum. With conditions similar to Chapter 2, we applied dispersive refractive index of gold in the simulations. Grid sizes are set as 1 nm because the penetration depth in gold is also about 10 nm at visible wavelengths. The simulation is performed with only one unit cell because periodic boundary conditions were used to effectively obtain the response of the entire periodic structures. The excitation source is set as plane wave with a pulsed temporal function for frequency analysis. The extinction which includes both the scattering and absorption can is directly related to the transmission. Dispersive spectrum can be obtained with Fourier analysis. The simulated extinction spectra of NP arrays are shown in Figure 3.2 (b). However, the simulated LSPRs of rectangular NPs are at slightly longer wavelength than measured LSPRs. To better match the simulated spectrum to the measured one, we also simulated the case for elliptical-shaped NP array to mimic the rounded edge of rectangle of real structure. A better match was seen with this modification.

To acquire information for both the phase and amplitude change of light passing through the arrays of rectangular shape gold NPs , we used SE in transmission mode at normal incidence in our experiment. SE measures the complex ratio of two orthogonal

transmission coefficients ρ of two orthogonally linear polarization states of light, with tan(ψ) representing the magnitude and Δ representing the phase angle of ρ. The measured results with different angles of orientation of rectangular NP arrays are shown in Figure 3.3. The angle of orientation (θ) of the rectangular NPs is defined as the angle between the shorter axis of rectangular NPs and the SE defined axis for the p-polarization.

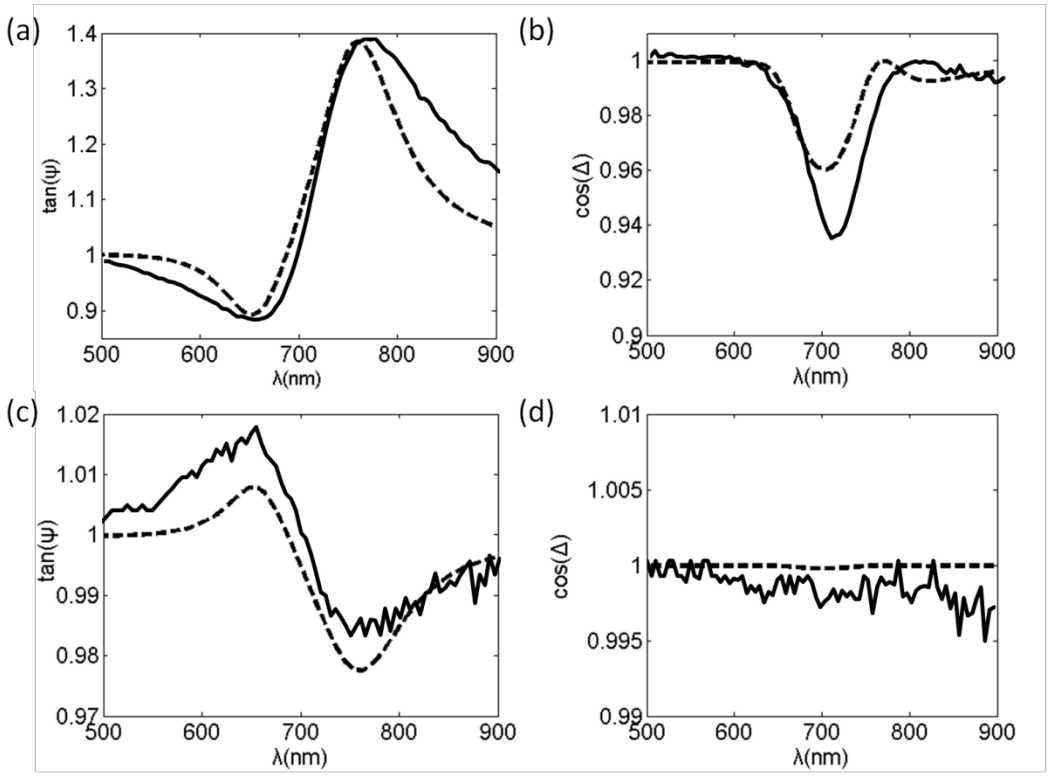

Figure 3.3Measured (solid) and calculated (dashed) curves of rectangular gold NP array for (a) tan(ψ) at θ = 0 degree, (b) cos(Δ) at θ = 0 degree, (c) tan(ψ) at θ = 45 degree, and (d) cos(Δ) at θ = 45 degree

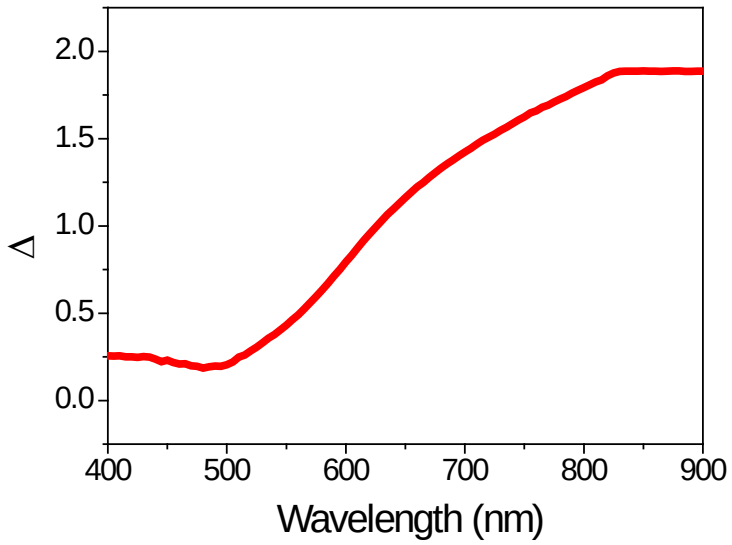

Figure 3.4Measured Δ of a diamond gold NP array shown in Figure 3.1 (a).

In order to interpret the measured SE results of the rectangular NPs, we modeled the optical transmission though the NP sample using Jones matrices as illustrated in Figure 3.5. The transmission coefficients through the NP sample are denoted as t_{Long} and t_{Short} for electric field polarized along the long and short axis of the rectangular NPs respectively. By appropriate coordinate transformations, the overall Jones matrix can be obtained and the complex ratio of two orthogonal transmission coefficients is given by Equation (3.1)

$$\rho = \tan\psi e^{i\Delta} = \frac{t_p}{t_s} = \frac{t_{\text{Short}}\cos^2\theta + t_{Long}\sin^2\theta}{t_{Short}\sin^2\theta + t_{Long}\cos^2\theta} \tag{3.1}$$

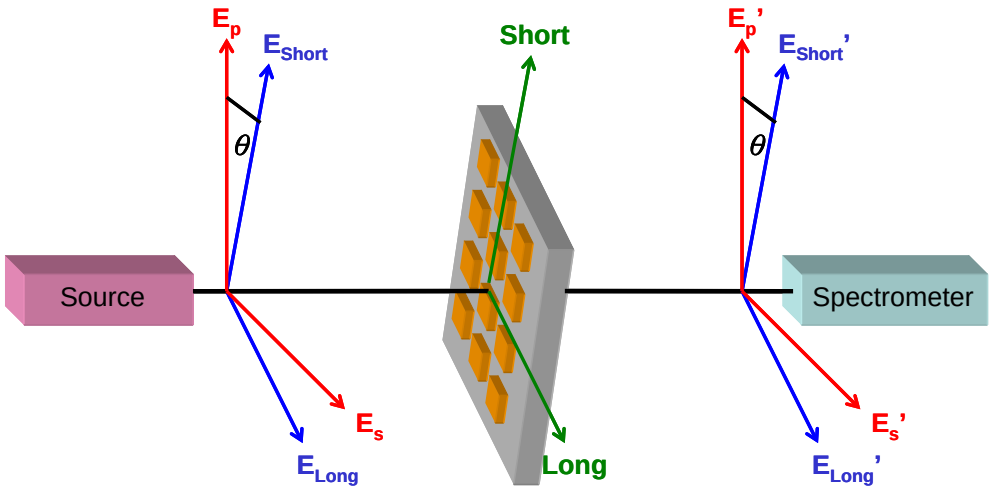

$$\begin{bmatrix} E_{Long} \\ E_{Short} \end{bmatrix} = \begin{bmatrix} \cos\theta & \sin\theta \\ -\sin\theta & \cos\theta \end{bmatrix} \begin{bmatrix} E_p \\ E_s \end{bmatrix} \qquad \begin{bmatrix} E_p' \\ E_s' \end{bmatrix} = \begin{bmatrix} \cos\theta & -\sin\theta \\ \sin\theta & \cos\theta \end{bmatrix} \begin{bmatrix} E_{Long}' \\ E_{Short}' \end{bmatrix}$$

$$\begin{bmatrix} E_{Long}' \\ E_{Short}' \end{bmatrix} = \begin{bmatrix} t_{Long} & 0 \\ 0 & t_{Short} \end{bmatrix} \begin{bmatrix} E_{Long} \\ E_{Short} \end{bmatrix}$$

Figure 3.5Configuration of transmission SE and construction of Jones matrices. E_p and E_s are the electric field components for the SE defined p and s polarizations. E_{Long} and E_{Short} are the electric field components polarized along the long and short axis of the NPs. θ is the angle of between E_p and E_{Short} or E_s and $t_{Long.}$ t_{Long} and E_{Short} are the complex transmission coefficients polarized along the long and short axis of the NPs.

Writing transmission coefficient *t* in the form of $e^{\alpha+i\delta}$ for both polarizations to account for the amplitude and phase change for light transmitted through the NP array, the real part of the exponent α_L and α_S polarized along the long and short axis can be extracted from the extinction spectra in Figure 3.2 (a). However the phase information cannot be obtained simply through measurement of extinction. We were interested to find out if the phase information can be obtained without the need of ellipsometry.

We noted that for the propagation through a homogenous medium, α and δ are both associated with the wavevector β because $\alpha+i\delta=i\beta d$, where d denotes the thickness of the medium. This equation can in turn be written as $\alpha+i\delta = i(1+ \chi'+i\chi'')^{1/2}\beta_0 d$, where χ'

and χ" denote the real and imaginary parts of the susceptibility and β_0 denotes the wavevector in free space. χ is small for many dielectric materials. The equation can be approximated by $\alpha+i\delta \approx (1+ \chi'/2+i\chi/2")\beta_0 d$ where $\alpha \approx -\chi/2"\beta_0 d$ and $\delta \approx (1+ \chi'/2)\beta_0 d$. From the Lorentz model described by Equation (A.13) we can see that the real χ' and χ" are related. It is well known that for any linear and causal systems, the real and imaginary part of the response can be related through Kramers-Kronig[88] relations given by Equation (3.2) and Equation (3.3)

$$\chi'(\omega) = \frac{-1}{\pi} P \int_{-\infty}^{\infty} \frac{\chi"(\omega)}{\omega' - \omega} d\omega' \tag{3.2}$$

$$\chi"(\omega) = \frac{1}{\pi} P \int_{-\infty}^{\infty} \frac{\chi'(\omega)}{\omega' - \omega} d\omega' \tag{3.3}$$

We treat the rectangular NP array as a metamaterial characterized by a homogeneous susceptibility χ because the ratio of the lattice constant (200nm) to the wavelength of interest (500 nm to 1000 nm) roughly meets the quarter wavelength homogeneity condition described in Chapter 2. From previous derivations, χ'' can be calculated from absorption coefficient α, and the χ' can be calculated through the use of Kramers-Kronig relations. Phase shift δ can thus be retrieved from χ'. With a complete description of transmission coefficients t_L and t_S, the complex ratio of two orthogonal transmission coefficients ρ and therefore tan(ψ) and Δ can be calculated. Using this model, excellent agreement between the measured and calculated results is shown in Figure 3.3. This model can help to understand of both amplitude and phase information from simple extinction measurement and Kramers-Kronig relations It can predict the

sensitivity of ellipsometrically probed LSPR to their structural characteristics and dielectric environments without using complicated instrumentation of ellipsometers.

The phase difference in rectangular NP array is relatively small due to the slight asymmetry of the structure. However, for the NP arrays of diamond shape as shown in Figure 3.1 (b), the optical response is quite different and strong in phase. In our measurement, Δ, the difference between phase shift in transmission coefficients of p-polarized and s-polarized light, can be larger than half π at near infrared as shown in Figure 3.4. As a comparison to the thickness of optical retarder made of crystal which is usually several microns thick, the thickness of NPs is only 20nm. The array diamond NPs thus can be potentially used to fabricate compact optical devices and find applications in integrated optics.

3.3 Conclusion

In this chapter, we were able to use NIL to fabricate various gold nanostructures exhibiting LSPRs with pronounced polarization dependence. We showed that SE is a very effective method to study the response in phase in addition to amplitude of the polarization dependent LSPR. Phase could bring up more information and further increase the sensitivity for LSPR-based sensing applications. The theoretical model described above can help to interpret measured results from SE and also predict the sensitivity of SE assisted LSPR sensing. Moreover, current LSPR sensing relies on monitoring the shift of the whole extinction spectrum in order to minimize the contribution due to external disturbances from background. SE can ratio out the external disturbance and profuce more reliable information for the LSPR spectrum. Polarization

dependent LSPR can further increase sensitivity by comparing LSPR specta at different polarizations as opposed to monitoring only one LSPR spectrum. Combining polarization dependent LSPR with SE can potentially yield a highly sensitive method for the detection of chemicals and biomolecules by acquiring complete amplitude and phase information of the LSPR. In addition, I would like to express my gratitude to Brandon Lucas for his contributions to this work.

Chapter 4

High Q Long-Range Surface Plasmon Polariton Modes in Sub-Wavelength Metallic Microdisk Cavity

4

4.1 Introduction

In the previous two chapters, we studied structures that have features much smaller than the wavelength. The electromagnetic properties of those structures are characterized by their effective parameters, scattering resonance, and absorption resonances. In this and the next chapter, structures of with features comparable to the wavelength are considered. Their electromagnetic properties, on the other hand, need to be treated with diffraction and geometrical optics. Nonetheless, these structures still respond to light in a much different way than large scale optical devices.

Subwavelength optical cavities are potentially useful as building blocks for integrated photonic circuits. For this purpose, it is highly desirable to scale the optical cavities to sub-wavelength in all three dimensions. Microdisk cavities have been proposed and investigated as sub-wavelength semiconductor lasers[89]. However, the lateral dimension of the traditional microdisk cavities is still limited to the scale of free space wavelength (λ_0) because large radiation (or scattering) loss in whispering-gallery mode (WGM) limits the attainable cavity Q factor when the disk diameter (D) is smaller than λ[90, 91]. Because metal can provide strong confinement of light which reduce

radiation loss, studies of metallic cavities have been rapidly growing in recent years in order to design deep sub-wavelength optical cavities. However, the loss introduced by metal limits the cavity Q factor below 300 for sub-wavelength metallic cavities[92-94]. The limit on cavity Q factor prevents such cavities to lase at room temperature. Efforts have been put to increase Q by incorporating low index materials[95, 96]. High Q semiconductor based sub-wavelength cavities are important for building electrically pumped lasers. In this chapter, we show that the Q of metal-capped semiconductor microdisk is primarily limited by metal loss; and introducing a novel structure of thin metal sandwiched between semiconductor disks would drastically reduce the metal loss and increase Q.

4.2 Q Factors of Microdisk Cavities

In traditional microdisk cavities the transverse confinement of the resonance modes is provided by the typical dielectric confinement of the air-cladded waveguide. To ensure that only the lowest order mode of the waveguide exists, the waveguide thickness need to be smaller than $\lambda_0/2n_s$ where n_s is the refractive index of semiconductor disk[97]. The effective refractive index (n_{eff}) of the lowest order waveguide mode is usually more than 1.5 times smaller than n_s. The reduction in n_{eff} introduces large radiation loss in WGM and cavity Q is reduced drastically especially for sub-wavelength diameter, D[98]. The metal-capped microdisk structure has been proposed to increase n_{eff} and therefore Q as illustrated in Figure 4.1 (a)[99]. For the surface plasmon polariton (SPP) guided WGM supported in the metal-capped microdisk cavity, waves are confined in the transverse dimension by the SPP mode at the metal-dielectric interface. As discussed in Chapter 1, the n_{eff} of the SPP mode is always larger than n_s and is thus much larger than the n_{eff} of

air cladded waveguide in traditional microdisks[100]. Therefore, the Q of WGM can be increased for subwavelength size cavities due to the improved optical confinement which minimizes the radiation loss. However, the additional metal loss experienced by SPP mode also puts a limit on the overall Q of SPP guided WGM. In the newly proposed structure illustrated in Figure 4.1 (b), the transverse confinement is provided by long-range surface plasmon polariton (LRSPP) confined in a thin metal film sandwiched between two layers of dielectrics with the same index. This LRSPP mode experiences a much lower metal loss and can elevate the limit on the Q of metallic microdisk cavity. To study the behaviors of the SPP as well as LRSPP guided WGM, we used the finite-difference-time-domain (FDTD) method to simulate the resonance behaviors and specifically the Q of proposed metallic microdisk structures.

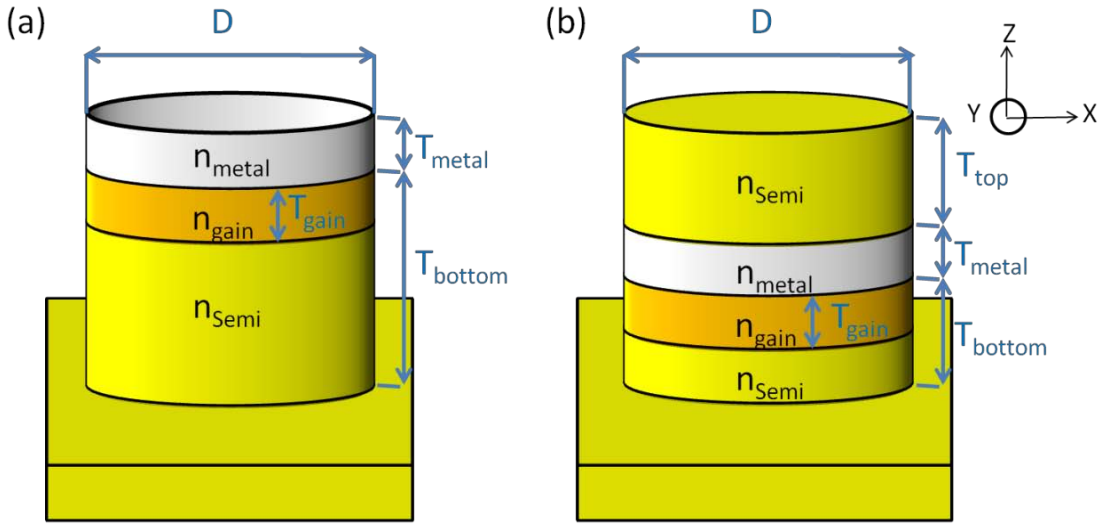

Figure 4.1(a) Metal-capped microdisk cavity supporting SPP guided WGM and (b) metal-sandwiched microdisk cavity supporting LRSPP guided WGM. T_{metal} and T_{gain} denote the thickness of Ag and Gain region. D denotes the disk diameter. T_{top} and T_{bottom} in (b) denote the thickness of GaAs disk above and beneath Ag layer respectively.

4.3 Simulation Conditions

The FDTD simulation is described with more details in Appendix The Finite-Difference-Time-Domain Method. The metal is chosen to be silver for minimizing the metal loss. The refractive index of metal nmetal is assigned as 0.13+10.1i for silver at λ=1400 nm[101]. The refractive of semiconductor nsemi is assigned as 3.4 for GaAs. In FDTD simulation, in order to resolve the smallest fields and structures the grid size needs to be 10 times smaller than both the effective wavelength (λ_0/neff) and the size of the smallest structures. In the lateral dimension, using a grid size of 30 nm fulfills the above two requirements for wavelength assumed as 1400 nm and D larger than 300 nm. In the transverse dimension, the grid size is chosen to be 2 nm in metal and 18nm in semiconductor considering that the penetration depth of SPP mode is 21 nm into silver and 184 nm into GaAs at λ_0 = 1400 nm. The source for exciting SPP mode is in TM polarization which has the transverse magnetic field component perpendicular to the metal-semiconductor interface and is placed at metal-semiconductor interface in order to excite SPP or LRSPP mode by end-fire coupling[102]. The temporal function of excitation is set as pulse for frequency analysis. Cavity Q factors can be calculated by estimating FWHM when Q is low and by complex frequency analysis when Q is high (over 1000) as discussed in Appendix The Finite-Difference-Time-Domain Method

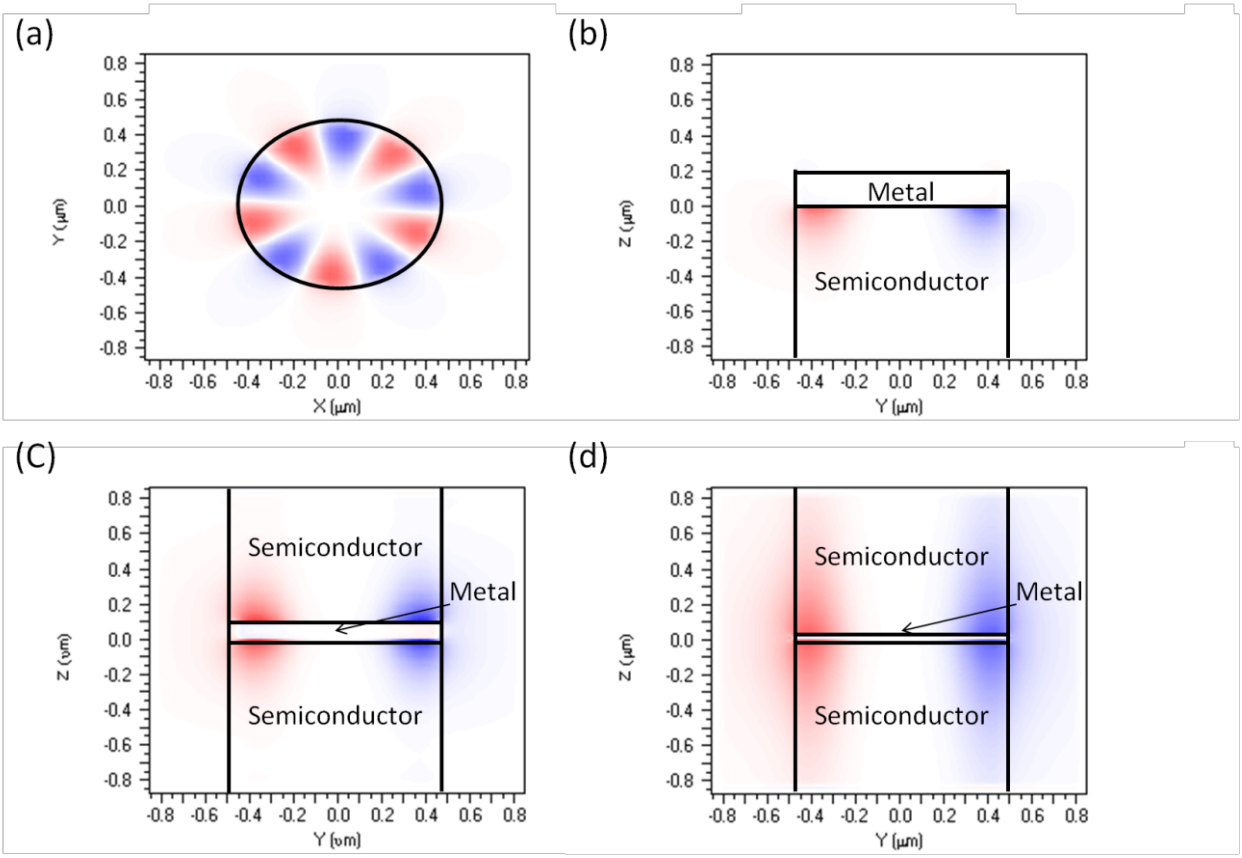

Figure 4.2(a) Lateral (Z = 0) and (b) transverse (X = 0) mode patterns of SPP guided WGM for the metal-capped structure depicted in Fig. 1a with infinite Tbottom. (c) Transverse (X =0) mode pattern of LRSPP guided WGM for the metal-sandwiched structure depicted in Figure 4.1(b) with T_{metal} = 100 nm and (d) with T_{metal} = 20 nm. T_{top} and T_{bottom} are assumed as infinite. The coupling between modes at two metal-semiconductor interfaces is stronger in (d) with a smaller T_{metal} than in (c) with a larger T_{metal}.

4.4 Metal-Capped Microdisk Cavity

Waves propagating in the metal-capped microdisk cavity depicted in Figure 4.1 (a) are simulated by FDTD. The thickness of metal layer Tmetal is assumed as 200 nm which is thick enough to prevent SPP mode at the metal-semiconductor interface from being coupled to the metal-air interface. We first consider a passive cavity by assuming the thickness of gain region Tgain as 0. We also ignore the radiation into substrate by assuming TBottom as infinite. Cavities with nonzero Tgain and finite Tbottom will be

studied in later sections. The mode profile in Figure 4.2 (a) reveals that the lateral confinement in x-y plane is provided by WGM just like in traditional microdisk cavities. On the other hand, the transverse mode profile in Figure 4.2 (b) reveals that the transverse confinement in the z dimension is provided by SPP mode with amplitude that peaks at metal-semiconductor interface and decays exponentially into both metal and semiconductor layers. In (a) Q of air-cladded waveguide guided, SPP guided, and LRSPP guided WGM with various T_{metal} versus disk diameter. T_{top} and T_{bottom} are assumed as infinite. The mode with smallest D/λ on each curve has a mode number m = 3. Mode difference between adjacent modes on each curve is 1. For T_{metal}=200 nm, the Q of LRSPP guided is identical to SPP guided WGM because there is no coupling between modes at two Ag-GaAs interfaces. (b) Q_{LRSPP} versus T_{metal}. (a), the simulated Q at λ0 = 1400 nm corresponding to the metal-capped microdisk cavity in Figure 4.1 (a) is compared with traditional microdisk cavity with air cladding. The thickness of traditional microdisk is assumed to be 200 nm which is just below $\lambda_0/2ns$ for ensuring single waveguide mode. The Q of SPP guided WGM, QSPP+WGM, is limited by two factors expressed in Equation (4.1) One is SPP limited Q, QSPP, which accounts for the metal loss experienced by the propagating SPP mode due to penetration into the metal layer. The other is WGM limited Q, QWGM, which accounts for the radiation loss experienced by WGM in the lateral direction.

$$\frac{1}{Q_{SPP+WGM}} = \frac{1}{Q_{SPP}} + \frac{1}{Q_{WGM}} \tag{4.1}$$

For D/λ below 0.7, the radiation loss is larger than the metal loss. $Q_{SPP+WGM}$ is primarily limited by Q_{WGM}. For D/λ above 0.7, the metal loss is larger than the radiation loss. The upper bound of $Q_{SPP+WGM}$ is Q_{SPP} independent of disk size. Q_{SPP} is 306 for Ag

and GaAs system at λ_0 = 1400 nm. On the other hand, the Q of air-cladded waveguide guided WGM is limited by radiation loss only. The effective index of air-cladded waveguide (n_{eff} = 2.74) is smaller than that of SPP mode (n_{eff} = 3.61) and introduces a large radiation loss of WGM. The metal-capped microdisk scales more favorably than the air-cladded microdisk for smaller size microcavities by providing higher Q's: as D/λ goes below 0.86, the overall Q of air cladded waveguide guided WGM drops below QSPP of the metal-capped microdiskas shown in Figure 4.1 (a). By using SPP transverse confinement, the radiation loss limited Q of traditional microdisk that exponentially depends on the diameter of microcavity is giving away to the metal-limited loss in SPP.

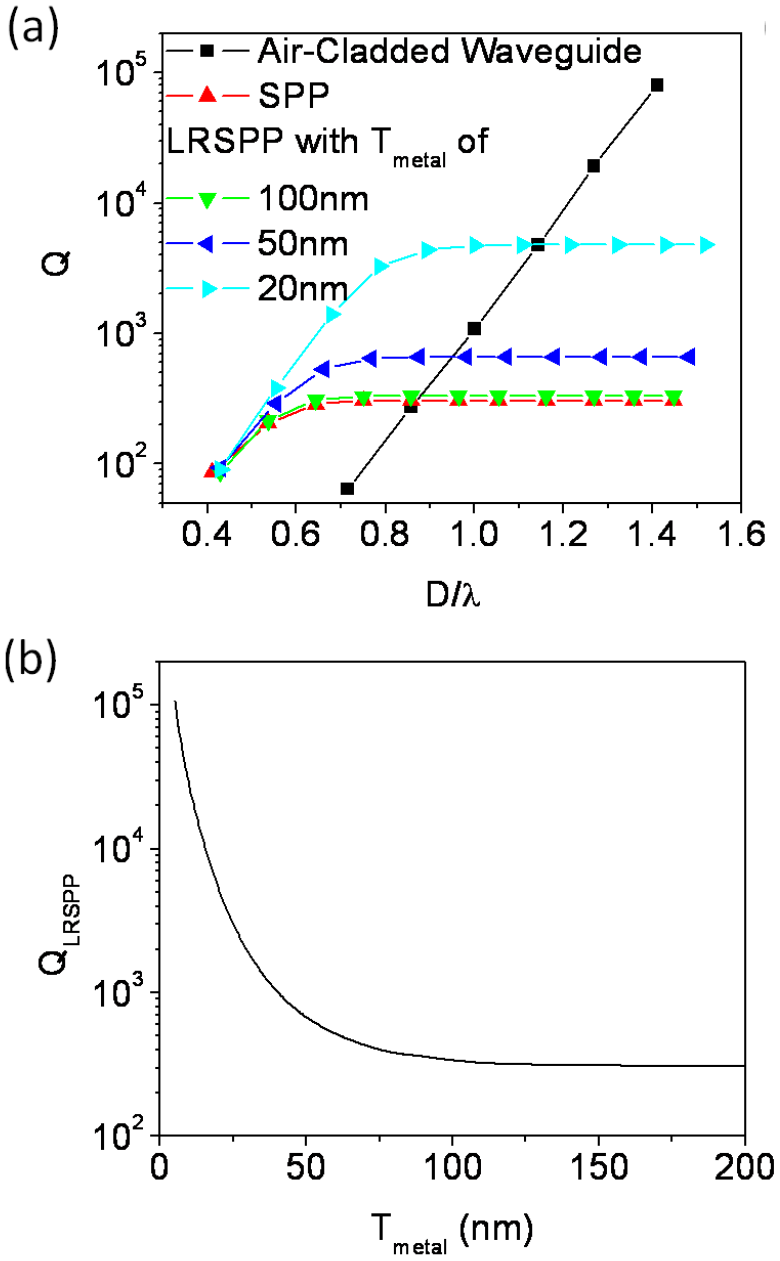

Figure 4.3 (a) Q of air-cladded waveguide guided, SPP guided, and LRSPP guided WGM with various T_{metal} versus disk diameter. T_{top} and T_{bottom} are assumed as infinite. The mode with smallest D/λ on each curve has a mode number m = 3. Mode difference between adjacent modes on each curve is 1. For T_{metal}=200 nm, the Q of LRSPP guided is identical to SPP guided WGM because there is no coupling between modes at two Ag-GaAs interfaces. (b) Q_{LRSPP} versus T_{metal}.

4.5 Metal-Sandwiched Microdisk Cavity

For metal-capped microdisk cavity, the Q is primarily limited by the metal loss which depends on the overlapping of electric field of the cavity modes with metal. The metal loss can be reduced by introducing LRSPP mode supported in a thin metal film sandwiched between identical semiconductor layers. The magnitude of metal loss is determined by the fraction of field inside the metal. LRSPP is the coupled mode of surface waves at two metal-semiconductor interfaces. When metal film is thick, surface waves propagating at two metal-semiconductor interfaces are not coupled and they propagate as two independent SPP modes. When metal film becomes thin, the two surface waves interact with each other and form a coupled surface plasmon mode. Such coupled surface plasmon mode has field penetrates more into bounding semiconductors. The penetration depth into GaAs is plotted against Ag thickness in Figure 4.3 (b) This results in the decrease of the fraction of field inside the metal and therefore the decrease of metal loss of such coupled mode[103], leading to longer propagation length and hence the name long-range SPP. The proposed metal-sandwiched microdisk structure depicted in Figure 4.1 (b) supports LRSPP in the transverse dimension by introducing a thin metal disk sandwiched between semiconductor disks. Again, we consider a passive cavity by assuming T_{gain} as 0 and ignore the radiation into substrate at bottom and air on top by assuming both T_{top} and T_{bottom} as infinite. Cavities with nonzero T_{gain}, finite T_{top} and finite T_{bottom} will be studied in later sections. The lateral mode pattern of metal-capped microdisk cavity has a WGM profile as in Figure 4.2 (a). The transverse mode profiles in Figure 4.2 (c) and Figure 4.2 (d) reveal that the LRSPP modes are coupled modes propagating at both metal-semiconductor interfaces. Thicker metal has weaker coupling

of two modes and less field penetration into semiconductor as show in Figure 4.2 (c). This leads to only a small amount of decrease of metal loss. Thinner metal has stronger coupling of two modes and more field penetration into semiconductor as show in Figure 4.2 (d). This leads to a larger amount of decrease of metal loss. In Figure 4.4 (a) the simulated Q at λ=1400 nm corresponding to the metal-sandwiched microdisk cavity is shown for different $T_{metal.}$ The cavity Q of LRSPP guided WGM for T_{metal}=200 nm coincides with SPP guided WGM because the surface wave at each interface propagates as uncoupled SPP mode for thick metal. Similar to SPP guided WGM, the Q of LRSPP guided WGM, $Q_{LRSPP+WGM}$, is limited by two factors expressed in Equation. (4.2)

$$\frac{1}{Q_{LRSPP+WGM}} = \frac{1}{Q_{LRSPP}} + \frac{1}{Q_{WGM}} \tag{4.2}$$

For D/λ below 0.7, $Q_{LRSPP+WGM}$ is also primarily limited by Q_{WGM} as in the case for $Q_{SPP+WGM}$. $Q_{LRSPP+WGM}$ is slightly smaller than $Q_{SPP+WGM}$ because of the smaller n_{eff} of LRSPP mode relative to SPP mode. For D/λ larger above 0.7, $Q_{LRSPP+WGM}$ is no longer capped by Q_{SPP} at about 310 as in the case of $Q_{SPP+WGM}$. Q_{LRSPP} keeps increasing as D/λ increases. The upper limit of $Q_{LRSPP+WGM}$ is set by Q_{LRSPP} which is larger with smaller T_{metal}. Figure 4.3 (a) Q of air-cladded waveguide guided, SPP guided, and LRSPP guided WGM with various T_{metal} versus disk diameter. T_{top} and T_{bottom} are assumed as infinite. The mode with smallest D/λ on each curve has a mode number m = 3. Mode difference between adjacent modes on each curve is 1. For T_{metal}=200 nm, the Q of LRSPP guided is identical to SPP guided WGM because there is no coupling between modes at two Ag-GaAs interfaces. (b) Q_{LRSPP} versus T_{metal}. (b) shows the Q_{LRSPP} with varying T_{metal}. This put an upper limit for $Q_{LRSPP+WGM}$ with fixed T_{metal}. For T_{metal} =20 nm, $Q_{LRSPP+WGM}$ can

reach about 4800. The range where cavity Q of metallic microdisk cavity is larger than traditional microdisk is expended for any microdisks with D/λ below ~1.15. The achievable $Q_{LRSPP+WGM}$ can be further increased by using smaller T_{metal}. As a comparison, cavity Q is about 270, 310, and 4400 for tradional microdisk, metal-capped microdisk, and metal-sandwitched microdisk with T_{metal} = 20 nm when D/λ is about 0.85.

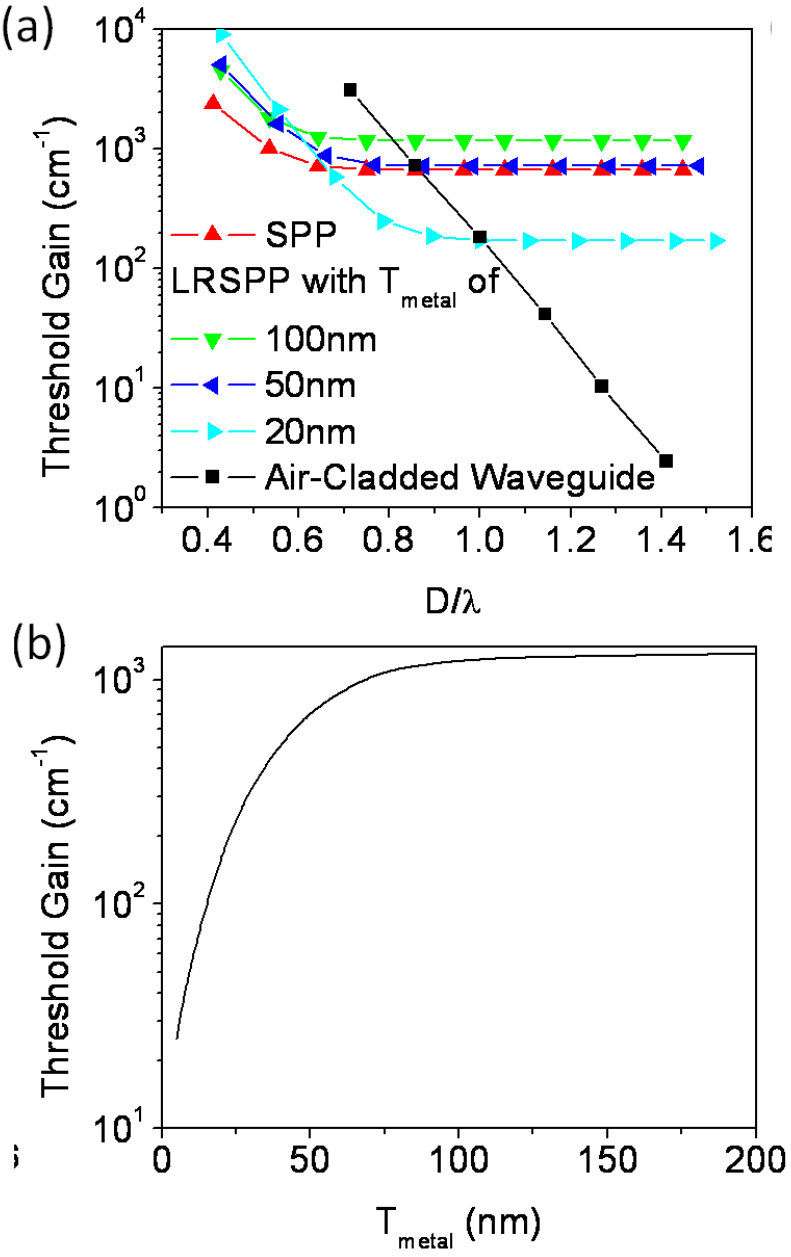

Figure 4.4(a) Threshold gain required for air cladding waveguide guided, SPP guided, and LRSPP guided WGM with various T_{metal} versus disk diameter. T_{top} and T_{bottom} are assumed as infinite. The mode with smallest D/λ on each curve has an azimuthal mode number m = 3. Mode number difference between adjacent modes on each curve is 1. (b) Threshold gain required for lossless propagation of LRSPP versus T_{metal}. T_{gain} is assumed as 100 nm.

4.6 Threshold Gain to Compensate Cavity Loss

When utilizing the cavity in laser, the threshold gain determines the lasing properties. The threshold gain required to compensate the cavity loss is not only related to the cavity Q but also the confinement factor of the mode in the gain region. For SPP and LRSPP modes, field peaks at metal-semiconductor interfaces. Placing the gain layer right next to the interface as shown in Fig. 4-1(a) and (b) can provide the largest confinement factor. For single mode waveguide, field peaks at the center of waveguide. Placing the gain layer at the center of air-cladded waveguide can provide the largest confinement factor. For LRSPP guided WGM, while Q increases with smaller T_{Ag}, the confinement factor decreases due to the larger penetration depth. The overall affect of varying T_{metal} on threshold gain can be studied by simulation. Figure 4.4 (a) shows the threshold gain for traditional microdisk with air cladding, metal capped microdisk, and metal sandwiched microdisk of various T_{metal}. The metal-capped microdisk has a lower threshold gain than traditional microdisk with air cladding for D/λ up to 0.85 because of the larger Q. However, for D/λ between about 1 and 1.15, although the metal-sandwiched microdisk with T_{metal} of 20 nm has a higher Q, the weaker confinement of LRSPP mode makes the threshold gain of metal-sandwiched microdisk larger. The metal sandwiched microdisk has a lower threshold gain than traditional microdisk with air cladding for D/λ up to 1 instead of 1.15.

Figure 4.4 (b) shows the required gain to compensate the propagation loss of LRSPP mode with varying T_{metal}. This required gain represents the lowest threshold gain of metal sandwiched microdisk with fixed T_{metal}. For T_{metal} larger than 50 nm, the lowest threshold gain is larger than that for metal-capped microdisk at about 670 cm^{-1}. This is because the

field existing in the top semiconductor layer reduces the confinement factor in the gain region. For T_{metal} smaller than 50 nm, the lowest threshold for metal sandwiched microdisk is smaller than metal-capped microdisk and can be reduced to about 170 cm^{-1} for T_{metal} of 20 nm. To illustrate the effectiveness of this approach, the threshold gain can be further reduced to 60 cm^{-1} and 25 cm^{-1} for T_{metal} of 10nm and 5nm. As a comparison, threshold gain is about 730 cm^{-1} and 670 cm^{-1} for traditional microdisk and metal-capped microdisk when D/λ is about 0.85. This reduction in threshold gain is crucial considering that the maximum modal gain achieved in QDs and QWs on GaAs substrate is about 50 cm^{-1} at wavelength above 1.3μm[104, 105].

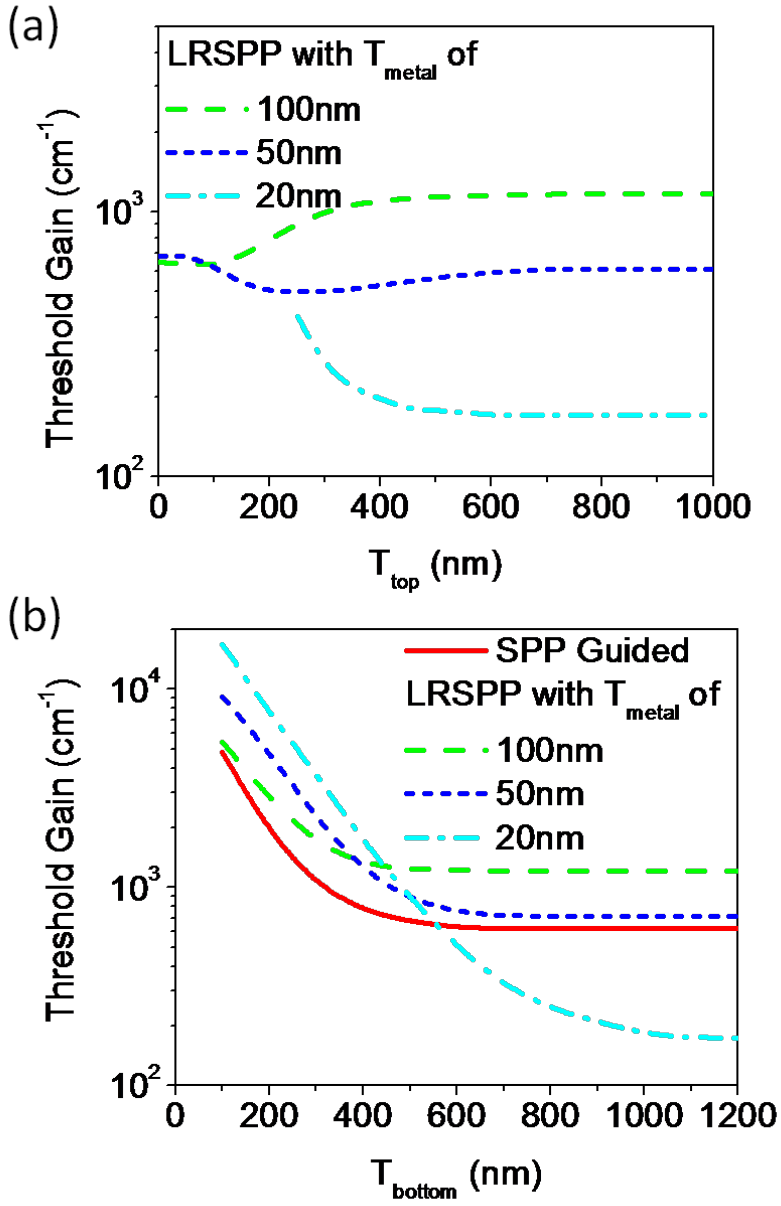

Figure 4.5Threshold gain of LRSPP guided WGM (a) versus T_{top}. (b) versus T_{bottom} for m = 8 assuming the thickness of gain region T_{gain} = 100 nm

4.7 Size Limit in the Transverse Direction

The above calculations are based on infinitely thick semiconductor disks. However, in order to achieve subwavength cavity in all three dimensions, we need to consider finite semiconductor layers T_{top} and T_{bottom} which can affect the transverse mode and the cavity

Q factor. In Fig. 4-5(a), cavity Q of LRSPP guided WGM is plotted against finite T_{top} while assuming infinite T_{bottom} with different T_{metal} for azimuthal mode number of 8 which has D/λ just below 1. Since the reduction of metal relies on the symmetry of the refractive indices of semiconductors on two sides of the metal, T_{top} need to be thick enough to provide the symmetry for LRSPP mode to exist. Threshold gain starts to approach the value for perfectly symmetric structure as shown in Fig. 4-4(b) when top semiconductor layer is thick enough for supporting LRSPP. Threshold gain approaches the value for SPP guide WGM when T_{Top} approaches 0 if metal is thick.

In Figure 4.5 (b), cavity Q of LRSPP guided WGM is plotted against finite T_{bottom} while assuming infinite T_{top} with different T_{metal} for mode number of 8. T_{bottom} needed to achieve minimum threshold gain is related to the penetration depth since cavity with smaller T_{bottom} causes larger radiation into GaAs substrate and increases the threshold gain. For T_{metal} of 20 nm, threshold gain smaller than 200 cm^{-1} can still be achieved for diameter of 1400 nm by choosing T_{top} of 400 nm and T_{bottom} of 900 nm for cavity size being subwavelength in all three dimensions.

4.8 Conclusion

In this chapter, we have analyzed the scaling property of novel metallic microdisk cavities. Simulation results tell us that metal-capped microdisk can provide larger cavity Q factor and lower threshold gain than the traditional microdisk cavity with air cladding when the disk diameter scales below wavelength. The cavity Q of metal-capped microdisk is primarily limited by the metal loss. LRSPP mode is known to have less overlapping electric field with metal which leads to the reduction of metal loss. Metal-sandwiched microdisk provides even larger cavity Q and lower threshold gain by

incorporating LRSPP. Cavity Q over 4000 and threshold gain below 200 cm^{-1} can be achieved for cavity size being subwavelength in all three dimensions with this type of novel microcavities. In Chapter 5, we will introduce another type of microdisk cavities that that could totally eliminate metal loss with purely dielectric structures.

Chapter 5

Photonic crystal microdisk lasers

5

5.1 Introduction

Microdisk and photonic crystal cavities have been investigated for sub-wavelength semiconductor lasers as the cavity modes have relatively high Q factor among all micron size cavities[89, 106, 107]. In Chapter 4, we discussed the design of microlasers using metallic microdisk cavities. In this chapter, we utilize photonic crystals instead of metals to provide light confinement in the transverse dimension for microdisk cavities.

The performances of microlasers not only relate to Q factor but also mode volume of the laser cavity. Cavity modes with a high Q factor and a small mode volume lead to a large Purcell factor and a low threshold modal gain for lasing[108]. In a microcylinder (e.g. a very thick microdisk), the mode area of Whisperirng Gallery Mode (WGM) in the lateral plane reduces linearly with the microdisk diameter[109]. However, the mode size of air-cladded waveguide mode in the transverse dimension does not scale linearly with the disk thickness and has a lower bound set by the scale of wavelength. One strategy to reduce the mode size in the transverse dimension is to introduce metallic coating on microdisk as described in Chapter 4 to support surface mode at the metal-dielectric interface or surface plasmon polariton (SPP) mode. Such surface mode is tightly bound to the metal-dielectric interface with decay lengths much smaller than the wavelength. The

small mode size of SPP mode leads to the small mode volume of the SPP-guided WGM. However, the loss introduced by metal sets an upper bound for the achievable Q factor of any SPP-guided modes including SPP-guided WGM. The achievable cavity Q factor is below 300 at any wavelengths below 1.5μm, which demands significant gain or pumping to lase. To produce surface wave, the most commonly used medium with negative real part of dielectric constant ε is metal, but the nonzero imaginary part of ε leads to metal absorption loss. In view of this, it is very attractive to consider photonic crystal (PC) structures made of dielectric materials, which can provide an equivalent ε purely negative inside the forbidden band[110]. This means that surface modes can also be supported at the interface of a dielectric PC and a uniform dielectric medium. More importantly, the propagation loss of such surface mode can be zero with the zero imaginary part of the effective ε, which leads to very sharp angular reflectivity resonances in experiments on prism-coupled excitation of surface waves in 1D PC[111]. The lossless propagation of surface mode in dielectric PCs offers the unique advantages for laser application over the SPP on metal surfaces. To create a small mode volume cavity with high Q factor, we designed stacked bilayers forming 1D PC along the transverse (i.e. vertical) dimension of microdisk cavity as illustrated in Figure 5.1 (a). Such surface mode guided WGM on PC microdisk can has a much higher Q factor than the SPP-guided WGM that suffers from the metal loss. Later in this chapter, we study their optical properties and demonstrate lasing in PC microdisk cavities fabricated on GaAs substrate with InGaAs quantum dots as gain media emitting at around 1μm.

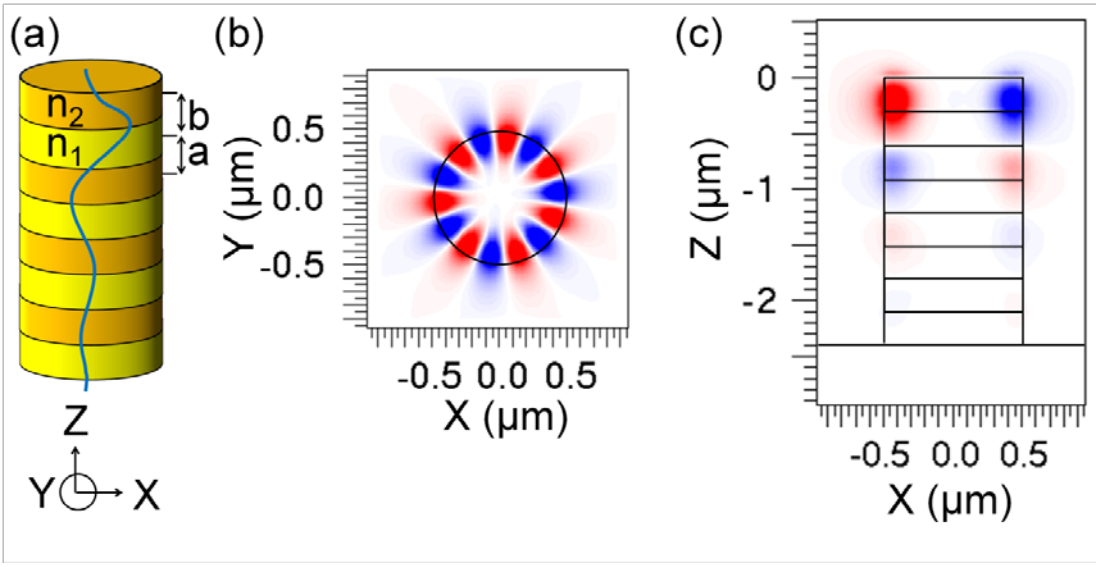

Figure 5.1(a) PC microdisk cavity supporting surface mode guided WGM. n1 and n2 denote the two refractive indices; a and b are the thickness of dielectric bilayers in each period of PC. The sketched curves represent the surface modes guided in the PC layers in the transverse direction. (b) The lateral and (c) transverse cavity mode profile (Hz) of the structure in (a) with four periods and disk diameter of 1000nm when n2 = 3.5, n1 = 3.1, and a = b =300nm.

5.2 Surface Mode Guided WGM

The properties of surface modes in 1D PC structure as depicted in Figure 5.1 (a) are studied by transfer matrix method calculations[112].The electromagnetic fields in each layer (unit cell) is represented by a incident wave and a reflected wave. By applying the boundary condition, the dispersive wavevector and field profiles can be found for each mode. The properties of PC microdisk cavities are studied by FDTD simulations. In all calculations and simulations, free space wavelength of 1000nm is assumed and n_1 and n_2 are assumed as 3.1 and 3.5 for $Al_{0.9}Ga_{0.1}As$ and GaAs at the wavelength of 1000nm. Surface mode can be guided only when the equivalent ε of PC is negative. The sign of equivalent ε at a specific wavelength is determined by the band structure plotted in Figure 5.2 (a) where a = b = 300nm is chosen for supporting surface mode with relatively large

effective index. A 1D PC with infinite number of periods can serve as a perfect Bragg reflector in the forbidden bands. Just like ideal metal can serve as a perfect reflector because of its purely negative ε, the perfect Bragg reflector formed by 1D PC also posses equivalent ε being purely real and negative in the forbidden bands, which leads to evanescent electromagnetic waves in the PC structure.

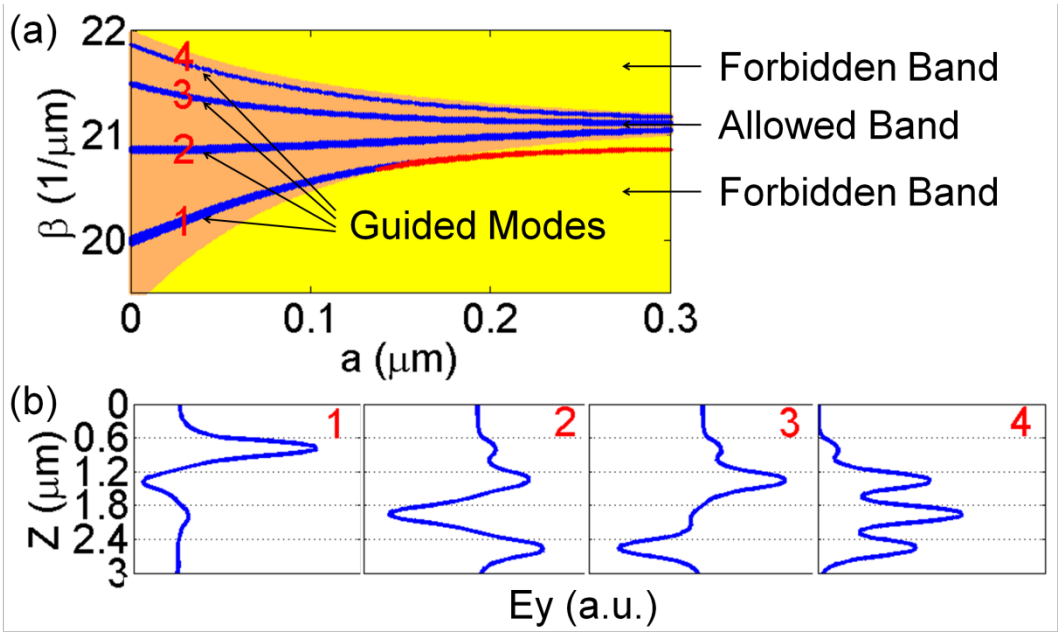

Figure 5.2(a) Band structure of infinite 1D PC for TE waves (electric field in y direction) n2 = 3.5, n1 = 3.1, and a = b = 300nm, where the forbidden and allowed bands are illustrated. The guided modes for finite 1D PC of four periods are illustrated by curves numbered from 1 to 4. (b) Transverse electric field distribution for each guided mode. For mode 1, 2, 3, and 4, the calculated mode sizes are 0.245λ, 0.482λ, 0.523λ, and 0.565λ and the confinement factors are 0.078, 0.017, 0.018, and 0.006 respectively.

The evanescent field profile of the surface modes is ideally suited to construct confined cavity modes for lasers. We now show that such mode in a cylindrical cavity provides the smallest mode volume while maintaining a large overlap with the gain media. For 1D PC with finite number of periods, apart from the surface modes in the

forbidden band, other propagating modes also exist in the allowed bands. Fig. 2(a) shows the dispersion curves for all guided modes in the first band of 1D PC with four periods, with the corresponding field profiles shown in Figure 5.2 (b). For 1D PC with N periods, there are N guided modes associated with each band. Within each forbidden band, there is at most one guided mode corresponding to the surface mode in 1D PC. Among these, the surface mode has the smallest extension in the transverse direction and this mode size is 0.245λ. The tight transverse confinement of the surface mode can help to reduce the overall cavity mode volume which in turn reduces the threshold modal gain. Moreover, since the modal gain is the product of material gain and confinement factor, a larger confinement factor leads to a lower threshold material gain for the same modal gain threshold required for lasing. The confinement factor of each mode is calculated by assuming four layers of gain material of 5nm thick with 10nm thick spacer placed at the center of the very top n_2 layer. It is found that the surface mode has a confinement factor of 0.078 which is at least four times larger than other guided modes in Figure 5.2 (b). This means that threshold material gain for surface mode is at least four times smaller than other guided modes. Although the propagation constant of surface mode is smaller than other guided modes and this could lead to a larger radiation loss, the reduction is at most 20% on the cavity Q factor for a microdisk of 1μm in diameter and can be well remedied by the larger difference in the confinement factor and mode size. In comparison, the fundamental mode size of a single disk layer of equal total thickness ($4 \times b$, where b is illustrated in Figure 5.1 (a)) is 2.6 times larger and the confinement factor is 3.3 times smaller the surface mode in PC cavity. The small mode volume and large confinement factor provided by surface mode in 1D PC makes it suitable for providing transverse

confinement for microdisk cavity. The cavity mode of PC microdisk is simulated by FDTD with lateral and transverse mode profile shown in Figure 5.1 (b). In FDTD simulations, grid size needed for resolving the smallest fields and structures can be released as opposed to simulations in Chapter 4 because there is no metal involed. A grid size 35 nm is set for all three dimensions considering $\lambda = \lambda_0/n = 285$ nm when $\lambda_0 =$ 1000nm and n = 3.5 for GaAs. The temporal function of excitation is set as pulse for frequency analysis. Cavity Q factors can be calculated by by complex frequency analysis because Q is high as discussed in Appendix The Finite-Difference-Time-Domain Method. The mode volume is only $0.05\lambda^3$ due to small mode size in the transverse direction and the cavity Q factor reaches over 30000, which is more than 100 times larger than metal-capped microdisk.

5.3 Experimental Demonstration of PC Microdisk lasers

To demonstrate the feasibility of semiconductor laser based on PC microdisk cavity, cavity structures were fabricated with four pairs of $Al_{0.9}Ga_{0.1}As$/ GaAs bilayers grown on GaAs substrate by MBE and with four InAs quantum dots layers embedded in the GaAs layers with a spacing of 15 nm. Microdisk cavities were patterned by electron-beam lithography and dry etched 2.5 μm deep to form four stacks of bilayers as illustrated in Figure 5.1 (a). The $Al_{0.9}Ga_{0.1}As$ layers are wet etched with buffered hydrogen fluoride (HF) to introduce larger index contrast with GaAs as shown in the inset of Figure 5.3. The fabricated PC microdisks were pumped by 780 nm pulsed laser with pulse width of 100fs and repetition rate of 80MHz. The surface mode in the transverse dimension could be excited by the spontaneous emission and form WGM in the lateral plane of the microdisk. The sample was cooled to 77 k in a liquid nitrogen cryostat. The emission

spectrum measured by InGaAs detector showed photoluminescence from InAs quantum dots centered at about 1μm. Development of peaks was observed for PC microdisks of diameter as small as 1.1μm (Figure 4.3). The sharp peak of width smaller than 1nm demonstrated the lasing behavior when power from pump laser is larger than 15 mW. The actual power absorbed by individual PC microdisk is much less.

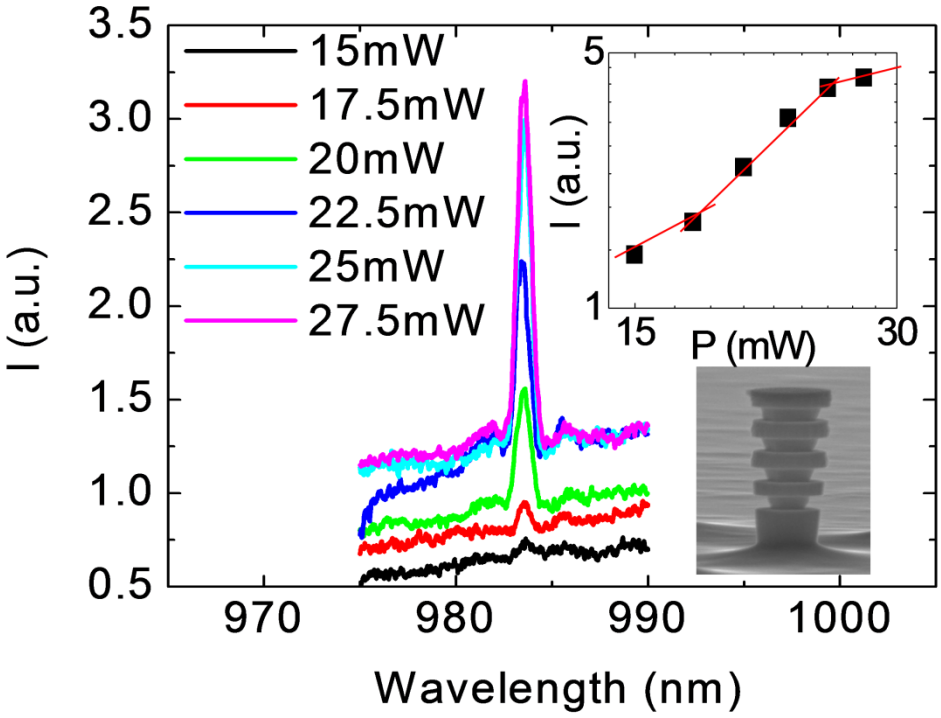

Figure 5.3Evolution of lasing peaks from PC microdisk with four layer of GaAs/AlGaAs (300nm thick for each layer) and diameter of about 1200nm. The inset shows peak intensity vs. pump power showing typical knee features; and a SEM photograph of the fabricated PC microdisk

5.4 Conclusion

In this chapter, we demonstrated another type of microdisk laser with transverse confinement provided by the PC surface mode and lateral confinement by WGMs. The surface mode supported by PC in the transverse dimension features small mode size, large confinement factor. However, as opposed to metallic microdisks discussed in

Chapter 4, there is no additional propagation loss other than the radiation loss of WGM in the lateral plane. The cavity mode in PC microdisk has low threshold material gain and therefore low threshold pump power. Our experimental results prove that such laser with structure sizes in all three dimensions about wavelength scale can lase at low pump power. Furthermore, I want to thank Yi-Kuei Wu for his efforts in completing this work together.

Chapter 6

Conclusion

6

6.1 Summary

In this dissertation, we have studied subwavelength optics in various aspects with structures of dimension range from deep subwavelength scales (Chapter 2 and Chapter 3) to scale comparable to wavelength (Chapter 4 and Chapter 5). The electromagnetic properties are treated with effective medium (Chapter 2), scattering by localized surface plasmons (Chapter 3), light confinement of propagating surface plasmons (Chapter 4), and feedback of photonic band gaps (Chapter 5). Potential applications of these structures include focusing and guiding of light (Chapter 2), sensing and microscopy (Chapter 3), and light sources (Chapter 4 and Chapter 5) for integrated optics. The realization of all these structures benefit from the advance in nanofabrication. We made use of the powerful and versatile FDTD method (Appendix The Finite-Difference-Time-Domain Method) to analyze the amplitude and phase responses of these structures in both time and frequency domain.

In Chapter 2, we studied artificial structures that generate induced the magnetic field and magnetic response for tailoring the permeability. Previous studies have shown that artificial structures made of split-ring resonators give negative permeability at microwave and infrared frequencies. We designed a new arrangement of SRRs that could lead to not

only negative permeability but also negative permittivity at visible frequencies. With this structure, negative refraction could be realized and applied with visible light. Perfect lenses constructed with negative index metamaterials could lead to deep subwavelength focusing. Moreover, the manipulation of light in nanoscale with metamaterials can be applied to subwavelength imaging and provide light guidance in optical circuits.

In Chapter 3, we researched the resonant scattering from metallic nanoparticles. This scattering is characterized localized surface Plasmon resonance and is sensitive to changes made to the particles. With the help of ellipsometry and FDTD, we were able to study their amplitude and phase response experimentally and numerically. We developed a model predict phase response directly from amplitude response of LSPR. Stable and high-sensitivity sensors could be realized based on this scheme.

In Chapter 4, we investigated the feasibility of scaling microcavities to subwavelnegth dimensions with metallic microdisks. Surface plasmon polariton modes existing in metallic structures could provide good confinement of light. The radiation from microdisk cavities can be reduced by depositing metal coating. However, additional loss is also introduced from metal absorption. We utilized thin metal supporting long range surface plason mode to reduce the metal absorption and could in turn successfully scale down the size of microcavities with substantially high cavity Q factor.

In Chapter 5, we utilized photonic crystals instead of metal to enhance the light confinement without suffering metal absorption. Inside the photonic bandgaps, surface modes can be guided to reduce the mode volume of microdisk cavities. Our proposed photonic crystal microdisk cavities have low threshold gain because of their high Q and small mode volume. We have demonstrated lasing from semiconductor laser cavities

based on this scheme. These subwavelength cavities could also find applications in other on-chip optical devices.

6.2 Outlook

In this dissertation, many promising features of these subwavelength structures have been studied. Nonetheless, there remain other variations of structures and phenomena are also worthwhile to study.

The SRR structure in Chapter 2 gives negative real part of refractive index. However, the imaginary part of refractive index is nonzero which leads to loss when light propagating through the structure. For an ideal negative refraction, lossless propagation is preferred. One possible way to compensate this loss is to incorporate material with gain with the structure[113]. Moreover, a real negative refraction is based on medium of large enough thickness. Adding SRRs in the third dimension should be considered to demonstrate negative refraction. This is can be done by adding additional layers of standing SRRs on top. The issues remained for investigation is how the magnetic resonances might be modified by the coupling between SRRs in adjacent layers and by the inclusion of gain medium to compensate the metal loss.

The optical properties of rectangular nanoparticles have been well studied in Chapter 3. However, the understanding for the response of diamond shape nanoparticles shown Figure 3.2 (a) is still not complete. The strong response in phase for diamond nanoparticles cannot be calculated from their amplitude response. Possible reasons include that the measured amplitude response outside of the range of spectrometer is also required for applying Kramers-Kronig relations; and the approximation $(1+\chi)^{1/2\approx}1+\chi/2$

may no longer be valid is χ is large. This could be understood first by simulating both the phase and amplitude response for further studies and other potential applications.

Although we have proposed a metal-sandwiched microdisk cavities giving high Q in Chapter 4, the fabrication of such structure is still a difficult task. Additional investigations for utilizing LRSPP for confining light in structures that are easier to make are worthwhile for demonstration of this idea experimentally.

In Chapter 5, the surface modes in photonic crystals were used to provide transverse confinement for microdisk cavities. Nonetheless, there are other modes not localized to the surface existing in photonic crystals as well. The studies of the interactions of these different transverse modes might also be valuable to obtain a complete understanding of this type of cavity and its lasing characteristics.

Appendix

The Finite-Difference-Time-Domain Method

A.1 Introduction

In this appendix, we will discuss the basic principles of the finite-difference-time-domain (FDTD) method which were used extensively in this dissertation using a commercial FULLWAVE package from the RSoft Design Group. Considering a linear, isotropic, nondispersive, lossless, and source free material, the Maxwell's curl equations from Faraday's Law and Ampere's Law are given by Equation (A.1) and Equation (A.2) $\vec{E}$ and $\vec{H}$ denote the electric and the magnetic field vectors. ε and μ denote the permittivity and permeability.

$$\frac{\partial \vec{H}}{\partial t} = -\frac{1}{\mu}\nabla \times \vec{E} \tag{A.1}$$

$$\frac{\partial \vec{E}}{\partial t} = \frac{1}{\varepsilon}\nabla \times \vec{H} \tag{A.2}$$

From Equation (A.1) and Equation (A.2) the scalar equations for the field vector components of in Cartesian coordinates are given by Equation (A.3) to Equation (A.8)

$$\frac{\partial H_x}{\partial t} = \frac{1}{\mu}\left[\frac{\partial E_y}{\partial z} - \frac{\partial E_z}{\partial y}\right] \tag{A.3}$$

$$\frac{\partial H_y}{\partial t} = \frac{1}{\mu}\left[\frac{\partial E_z}{\partial x} - \frac{\partial E_x}{\partial z}\right] \tag{A.4}$$

$$\frac{\partial H_z}{\partial t} = \frac{1}{\mu}\left[\frac{\partial E_x}{\partial y} - \frac{\partial E_y}{\partial x}\right] \tag{A.5}$$

$$\frac{\partial E_x}{\partial t} = \frac{1}{\mu}\left[\frac{\partial H_z}{\partial y} - \frac{\partial H_y}{\partial z}\right] \tag{A.6}$$

$$\frac{\partial E_y}{\partial t} = \frac{1}{\mu}\left[\frac{\partial H_x}{\partial z} - \frac{\partial H_z}{\partial x}\right] \tag{A.7}$$

$$\frac{\partial E_z}{\partial t} = \frac{1}{\mu}\left[\frac{\partial H_y}{\partial x} - \frac{\partial H_x}{\partial y}\right] \tag{A.8}$$

With this set of equations, the time derivative of each $\vec{E}$ component can be calculated from the space derivatives of the $\vec{H}$ components and vice versa. The Yee algorithm places the $\vec{E}$ and $\vec{H}$ components in a three-dimensional space in a interlaced manner such that each $\vec{E}$ component is surrounded by four $\vec{H}$ components and vice versa as shown in Figure A.1.

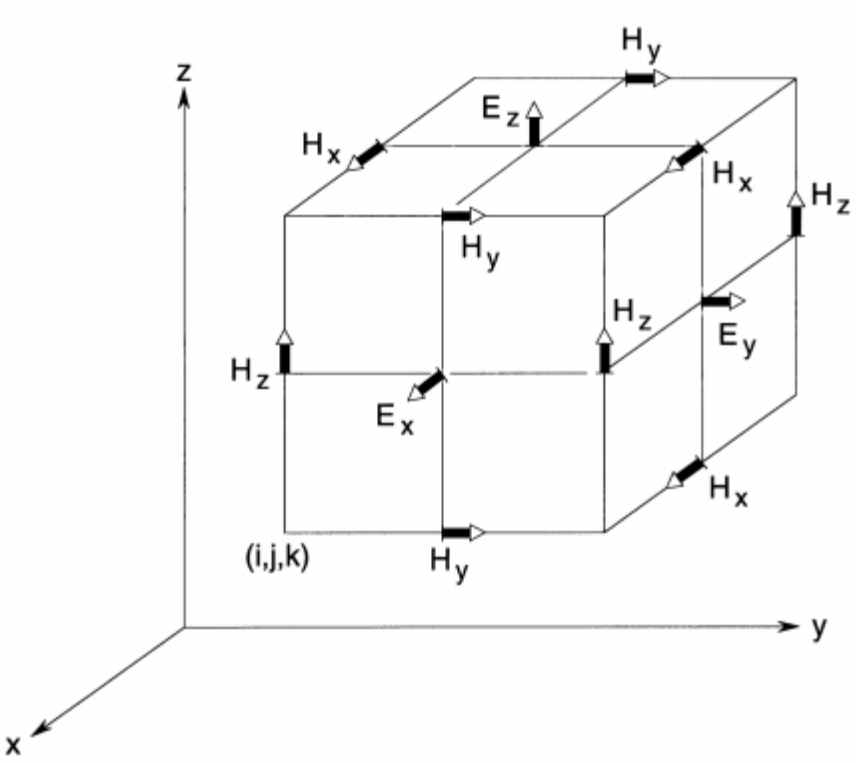

Figure A.1The position of $\vec{E}$ and $\vec{H}$ components in a Yee cell. The grid points of $\vec{H}$ components are shifted half grid spacing from the $\vec{E}$ components. Two adjacent grid points of each field vector component are separated by Δx, Δy, or Δz[25].

Using central-finite difference expressions for the space and time derivatives, Equation (A.3) and Equation (A.6) can be written as Equation (A.9) and Equation (A.10) where (i, j, k) denote a space point (iΔx, jΔy, kΔz) in Cartesian coordinates and n denotes a time point nΔt. The remaining four scalar equations can also be written with central-finite difference expressions in similar ways.

$$\frac{H_x\Big|_{i-\frac{1}{2},j+1,k+1}^{n+1} - H_x\Big|_{i-\frac{1}{2},j+1,k+1}^{n}}{\Delta t} = \frac{1}{\mu}\left[\frac{E_y\Big|_{i-\frac{1}{2},j+1,k+3/2}^{n+1/2} - E_y\Big|_{i-\frac{1}{2},j+1,k+1/2}^{n}}{\Delta z} - \frac{E_z\Big|_{i-\frac{1}{2},j+3/2,k+1}^{n+1} - E_z\Big|_{i-\frac{1}{2},j+1/2,k+1}^{n}}{\Delta y}\right] \tag{A.9}$$

$$\frac{E_x\Big|_{i,j+1/2,k+1/2}^{n+1/2} - E_x\Big|_{i,j+1/2,k+1/2}^{n-1/2}}{\Delta t} = \frac{1}{\mu}\left[\frac{H_y\Big|_{i,j+1/2,k+1}^{n} - H_y\Big|_{i,j+1/2,k}^{n}}{\Delta z} - \frac{H_z\Big|_{i,j+1,k+1/2}^{n} - H_z\Big|_{i,j+1,k+1/2}^{n}}{\Delta y}\right] \tag{A.10}$$

Using all the six central-finite difference expressions derived from Equation (A.3) to Equation (A.8) the value of each $\vec{E}$ component at time t=(n+1/2)Δt can be calculated from its previous value at time t=(n-1/2)Δt and the previous values of $\vec{H}$ components at adjacent points at time t=(n)Δt. Similarly, the value of each $\vec{H}$ component at time t=(n+1)Δt can be calculated from its previous value at time t=(n)Δt and the previous values of $\vec{E}$ components at adjacent points at time t=(n+1/2)Δt. Based on this leapfrog arrangement in time (Figure A.2), all the $\vec{E}$ and $\vec{H}$components at any discrete points in the space and time can be computed once the initial values are set. Thus, the physical

propagation of electromagnetic waves through any media can be modeled in a nature manner by the numerical propagation of electromagnetic waves at discrete points.

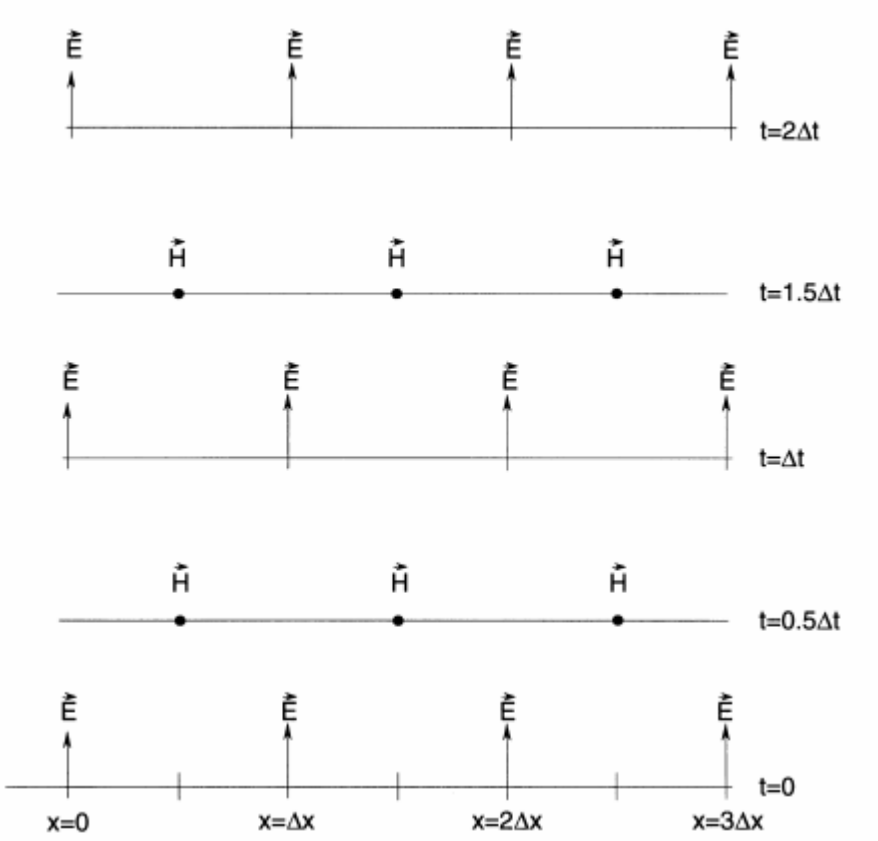

Figure A.2The space-time chart of the Yee algorithm. $\vec{E}$ and $\vec{H}$ are separated by Δt/2 and Δx/2 with each other to be applied with central-difference approximations[25].

Although the FDTD method is a powerful and nature way to deal with the interactions between electromagnetic waves with matters, special cares for performing accurate and effective simulations will be discussed in the following sections.

A.2 Spatial Grid Sizes and Time Step

The central-difference approximations used in the FDTD algorithm are second-order accurate. The simulated results deviate more from the exact solutions when the errors from the approximations increase. The errors generally decrease with the spatial grid

sizes and the time step. The spatial grid sizes (Δx, Δy, and Δz) generally need to be ten times smaller than the principle wavelength of interest in the material to resolve the smallest features of the electromagnetic fields. Moreover, for some structure of feature size much smaller than the scale of the wavelength , the spatial grid size sometimes need to be further reduced to resolve the geometrical details of the structures. Once the spatial grid sizes are set, in order to perform a stable simulation, there is an upper stable limit for the time step (Δt) set by the Courant condition given in Equation (A.11) For any simulations using Δt larger than the stable limit, it is certain that the computed values will grow exponentially in time. This exponential growth is the result of the introduction of a negative imaginary part of frequency to the numerical propagation of electromagnetic waves[25, 114].

$$\Delta t \leq \frac{1}{c\sqrt{\frac{1}{(\Delta x)^2}+\frac{1}{(\Delta y)^2}+\frac{1}{(\Delta z)^2}}} \tag{A.11}$$

Although simulations tend to be more accurate with smaller spatial grid sizes and time step, there is a tradeoff between performing accurate and effective simulations. The memory required to store the values of all field vector components at all the spatial grid points will substantially increase as the grid sizes decrease. The number of computations required for the numerical propagation of electromagnetic waves of a certain length in time will also increase as the time step decreases. The increase of computational memory and computational steps will require a larger computational power or a longer computational time for the simulation. Therefore, a conversion study usually needs to be performed for each type of simulations, especially for three-dimensional simulations

which usually require substantial amount of time. The split-ring resonators (Chapter 2), metallic nanoparticles (Chapter 3), and metallic microdisks (Chapter 4) all involve plasmonic effects with metals. As mentioned previously, both propagating surface plasmons and localized surface plasmons have strong field localization to the surface of metal. The penetration depth in the metal is usually more than ten times smaller than the free space wavelength. Thus, it is desired to use spatial grid sizes even smaller than the penetration depth to resolve the features of electromagnetic fields. Nonetheless, to perform an effective simulation, we usually tested a set of simulations with varying spatial grid size in each dimension. The maximum spatial grid size in each dimension to obtain results within acceptable deviations can be determined. Other simulations of the same type can be performed using these maximum grid sizes for obtaining accurate results with the minimum computational power and computational time.

In some cases that the orthogonal, regular Cartesian grids do not lead to accurate and efficient simulations, some alternative grids might be preferred. One type of alternative grids is the nonuniform orthogonal grid. Some geometry requires small spatial grid sizes in some regions of the simulation domain near small geometrical features to accurately resolve the electromagnetic fields localized to these regions. However, the spatial grid sizes can be released in other regions of the simulation domain. Using uniform grids would be an unnecessary waste of computational effort and resource because not the whole simulation domain requires such small grids. More efficient simulations can be performed using nonuniform grids[115-117] to avoid computational waste in the regions where small spatial grid sizes are not necessary. In the case of metallic structures, small spatial grid sizes need to be used near the surface of metal to resolve the features of

localized fields but most of the other regions in the simulation domain do not require such small spatial grid sizes. Figure A.3 displays the nonuniform grid used in the metal-capped microdisk cavity corresponding to Figure 4.2(b). At the free space wavelength λ_0 = 1400 nm, the wavelength in the semiconductor $\lambda = \lambda_0/n_{semi}$ = 417 nm. The penetration is 21 nm in the metal and 184 nm in the semiconductor. The spatial grid size in the lateral dimensions only need to be ten times than the wavelength which is 417 nm in semiconductor and 1400 nm in free space so we chose $\Delta x = \Delta y$ = 40 nm inside the microdisk (0.5 μm < X < 0.5 μm) = and $\Delta x = \Delta y$ = 140 nm elsewhere. The spatial grid sizes in the transverse dimension need to be ten times than the penetration depth which is 21 nm in metal and 184 nm in the semiconductor so we chose Δz = 2 nm in the metal (0 < Z < 0.1 μm) and Δz = 18 nm in the semiconductor (X < 0). Using a nonuniform grid in this metal-capped microdisk saved us about 95% of simulation time when using a uniform grid.

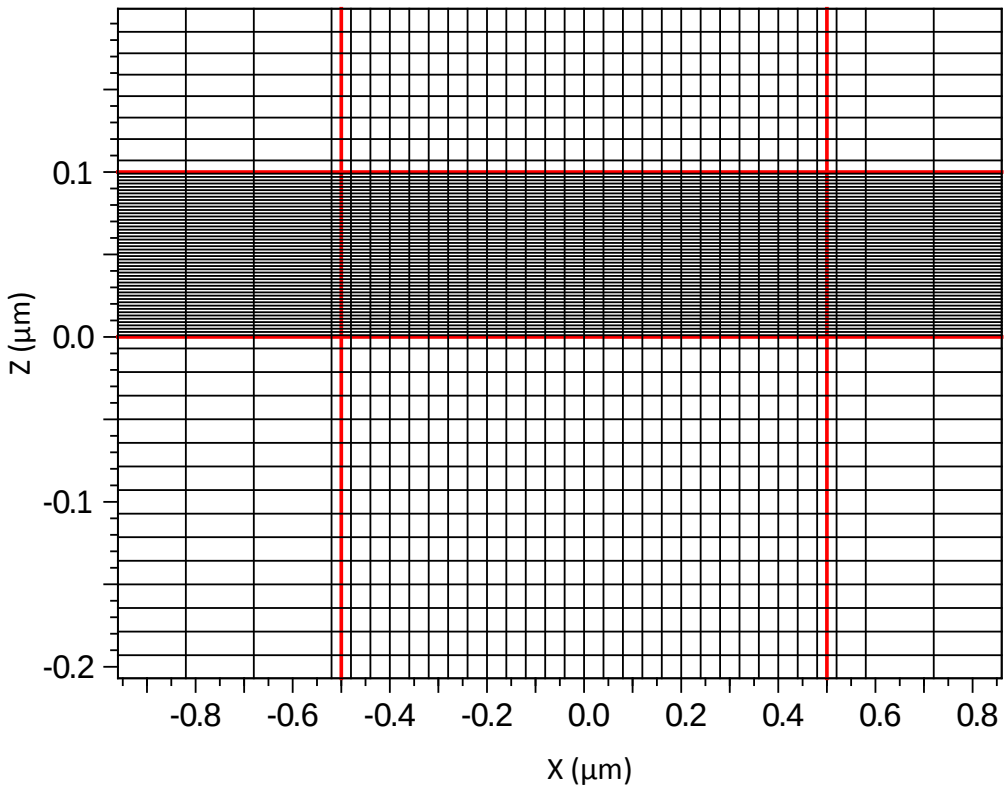

Figure A.3A nonuniform grid corresponding to Figure 4.2 (b) at X = 0. The range of Z axis is reduced to show the refined Δz in the metal

A.3 Boundary Conditions

In many cases, the structure of interest is in an unbounded spatial domain. However, it is not realistic to set the simulation domain infinitely large as this will require unlimited amount of memory. A reasonable simulation domain should be finite in size and enclose the structures of interest. A preferred boundary condition of the finite simulation domain should mimic an infinitely large domain. An infinitely large domain can be mimicked with a boundary which can suppress all reflections as if all the outward propagating waves are able to exit without boundary. This can be realized with an absorbing boundary

condition. The most efficient way to achieve an absorbing boundary condition is to use an absorbing material at the boundary. The impedance of this absorber is perfectly matched to the host medium which acts as a highly lossy material that absorbs all incident electromagnetic waves. The width of the perfectly matched layer needs to be smartly chosen so that it wide enough to effectively absorb incident energy but not too wide to unnecessarily increase the simulation domain.

In other cases, the structure of interest is periodic in one or multiple dimensions. When the structure contains infinite or a large number of periods, the simulation domain enclosing the whole structure can be too large for affordable computational power and time. One way to resolve this issue is to simulate only unit cell of the periodic structure with periodic boundaries which assume that electromagnetic waves leaving the boundary on one side of the unit cell should reenter the unit cell from the opposite side. We used periodic boundaries for periodic metallic nanoparticles in Chapter 3 and periodic split-ring resonators in Chapter 2.

A.4 Excitation Sources

Another fundamental aspect of the FDTD algorithm is the implementation of appropriate excitation sources to interact with the structure of interest. Each excitation source should contain both the spatial and time functions.

There are three common types of spatial excitations. (1) $\vec{E}$ and $\vec{H}$ field excitations simulate incident beams in the real world and are the most common type of excitation sources. We also used $\vec{E}$ and $\vec{H}$ field excitations for all simulations presented in this dissertation. (2) $\vec{J}$ and $\vec{M}$ current excitations can deposit charge and generate fields associated to charge because fields are produced though $\vec{J}$ and $\vec{M}$ terms in Maxwell's curl

equations from Faraday's Law and Ampere's Law are given by Equation (A.1) and Equation (A.2) (3) Enclosed excitations allow arbitrary plane-wave propagation inside an enclosed volume. It assumes that the incident and scattered fields can be separated. Both the incident and scattered fields are stored inside the enclosed volume but only the scattered fields are stored outside the enclosed volume. Thus, enclosed excitations can facilitate the calculations for scattering. The profiles and the positions of field excitations can also affect the results of FDTD simulations. We used plane waves placed external to the structures to obtain the transmission and reflection coefficients in Chapter 2 and Chapter 3. We placed TM polarized Gassian beams at the metal-dielectric interface to excite surface plasmon polaritons along the metal-dielectric interface by mimicking the end-fire coupling in Chapter 4[102]. In Chapter 4 and Chapter 5, when we placed Gaussian beams between the center and the circumference of microdisk cavities and let the beams propagate in-plane, whispering gallery modes can be excited as well.

The time function of an excitation sources can be a continuous wave, a pulse, or a impulse. A continuous wave excitation is used when a steady state solution is desired at a specific wavelength. Field distributions in the nanostructures in Chapter 2 and Chapter 3 can be obtained with a continuous wave excitation. A pulse excitation is used when a frequency dependent result is desired. Time transmission and reflection spectrum are obtained from the time dependent transmission and reflection coefficients by Fourier transform with pulse excitations in Chapter 2 and Chapter 3. The cavity modes within a certain frequency band can also be found in the radiation spectrum of the cavities in Chapter 4 and Chapter 5. An impulse excitation is used when trying to search for cavity modes at all frequencies. It is worthwhile to note that in some cases, the temporal

responses die out in time fast. Adding padding factors to the simulation could mimic longer numerical electromagnetic wave propagation and help to increase the resolution of the frequency responses.

A.5 Material Properties

As mentioned in the previous section, frequency responses can be obtained from the FDTD simulations. The dispersive material parameters should also be considered when dealing with dispersive media. Metals, for example, are highly dispersive media. In order to incorporate the dispersive material properties, the temporal response need to be first obtained from the frequency response by inverse Fourier transform. Inverse Fourier transform from the frequency to time domain requires the material response across the whole spectrum which might be hard to measure. Fortunately, most material properties are determined by the susceptibility and the dispersive susceptibility ($\chi = \varepsilon - 1$) can usually be modeled with Lorentz functions given by Equation (A.12) where ω is the angular frequency, N is the number of pole pairs, ω_p is the undamped resonant frequency, δ_p is the damping coefficients, and $\Delta\varepsilon_p$ is the change of relative permittivity due to the Lorentz pole pair[25]. From this explicit expression of the frequency response $\chi(\omega)$, the temporal response $\chi(t)$ can obtained and incorporated in the FDTD simulations. The dispersive material parameters are based on Reference [118]. In Chapter 4, we also incorporated gain media to simulate the threshold gain for the microdisk cavities. A gain medium can be easily assigned with a negative imaginary part of susceptibility while a lossy materials has a positive imaginary part of susceptibility

$$\chi(\omega) = \sum_{p=1}^{N} \frac{\Delta\varepsilon_p \omega_p^2}{\omega_p^2 + 2j\omega\delta_p - \omega^2} \tag{A.12}$$

A.6 Finding Cavity Q Factors

In Chapter 4 and Chapter 5, we calculated the cavity Q factors which can be used to calculate the total cavity loss. There are several different representations of the cavity. Three of those representations given by Equation (A.13) Equation (A.14) and Equation (A.15) are commonly used in the FDTD simulations for calculating the cavity Q factor, where α is the energy decay rate with time.

$$Q = \frac{\omega}{\Delta\omega_{FWHM}} \tag{A.13}$$

$$Q = 2\pi \frac{Energy\ Stored}{Energy\ Dissipated\ per\ Optical\ Cycle} \tag{A.14}$$

$$Q = 2\pi \frac{\omega}{\alpha} \tag{A.15}$$

With Equation (A.13) the cavity Q factor can be calculated by finding the FWHM of the mode peak in the spectrum. This is a simple way of calculating the cavity Q factor. However, if the cavity Q factor is high, the FWHM can be very narrow and a high frequency resolution is needed to resolve the narrow FWHM. Yet, to achieve a high frequency resolution, the computational time might be unreasonably long.

With Equation (A.14) the cavity Q factor can be calculated with two quantities: energy density and the radiation power. However, the radiation power only accounts for the energy dissipated by radiation. The energy dissipated by material absorption cannot

be obtained from the FDTD simulations. The cavity Q factor of metallic microdisk cavities cannot be accurately calculated using Equation (A.13)

With Equation (A.15) the cavity Q factor can be obtained from a single quantity: the energy decay rate which can be extracted from the time-dependent energy density. This is the most practical way to calculate the cavity Q factor among these three.

Last but not least, there is a more efficient way to accurately calculate the cavity Q factor with some more complexity. The goal is to solve the complex frequencies of cavity modes of a finite number instead of the virtually continuous spectrum of the real value frequency. Using nonlinear fit instead of Fourier transform, these complex frequencies can be calculated. The imaginary part of each complex frequency is associated to the decay rate of each cavity mode. Using this method, the cavity Q factors are usually calculated accurately within a shorter computational time. The accuracy of above mentioned methods mostly rely on the computational time, the convergence study on not only the spatial grid size but also the total computational time is necessary. Similar to the discussions in section A.2, a minimum computational time for achieving comparable accuracy was obtained first. Other simulations of the same type may use the same conditions to accurately calculate the cavity Q factors.

A.7 Conclusion

The FDTD algorithm provides an intuitive way to simulate the propagation of physical electromagnetic waves with numerical electromagnetic waves. Since the FDTD algorithm is based on central-difference approximations in the space and time, the accuracy of the algorithm depends on the settings of the spatial grids and time steps. By varying the boundary conditions and excitation sources, various types of simulations can

be performed. Not only the time dependent responses but also the frequency dependent responses can be obtained from the FDTD simulations. Despite few limitations arising from the limited computational power, FDTD is a generally versatile method for treating electromagnetic problems.

BIBLIOGRAPHY

1. Barnes, W.L., A. Dereux, and T.W. Ebbesen, Surface plasmon subwavelength optics. Nature, 2003. 424(6950): p. 824-30.

2. Brongersma, M.L. and P.G. Kik, Surface plasmon nanophotonics. Springer series in optical sciences. 2007, Dordrecht: Springer. vii, 268 p.

3. Kirchain, R. and L. Kimerling, A roadmap for nanophotonics. Nature Photonics, 2007. 1(6): p. 303-305.

4. Maier, S.A., Plasmonics - Towards subwavelength optical devices. Current Nanoscience, 2005. 1(1): p. 17-23.

5. Prasad, P.N., Nanophotonics. 2004, Hoboken, NJ: Wiley. xv, 415 p.

6. Shalaev, V.M. and S. Kawata, Nanophotonics with surface plasmons. 1st ed. Advances in nano-optics and nano-photonics,. 2007, Amsterdam ; Boston: Elsevier. xiv, 325 p.

7. Shen, Y.Z., et al., Nanophotonics: Interactions, materials, and applications. Journal of Physical Chemistry B, 2000. 104(32): p. 7577-7587.

8. Willets, K.A. and R.P. Van Duyne, Localized surface plasmon resonance spectroscopy and sensing. Annual Review of Physical Chemistry, 2007. 58: p. 267-297.

9. Shalaev, V.M., Optical negative-index metamaterials. Nature Photonics, 2007. 1(1): p. 41-48.

10. Bohren, C.F. and D.R. Huffman, Absorption and scattering of light by small particles. 1983, New York: Wiley. xiv, 530 p.

11. Mishchenko, M.I., L.D. Travis, and A.A. Lacis, Scattering, absorption, and emission of light by small particles. 2002, Cambridge ; New York: Cambridge University Press. xv, 445 p., [16] p. of plates.

12. Rayleigh Scattering. 1982, University of Michigan. Radiation Laboratory: [Ann Arbor, Mich.].

13. Hightower, R.L. and C.B. Richardson, Resonant Mie scattering from a layered sphere. Appl Opt, 1988. 27(23): p. 4850-5.

14. Guo, W., Light-scattering theory of diffraction. J Opt Soc Am A Opt Image Sci Vis, 2010. 27(3): p. 492-4.

15. Joannopoulos, J.D., Photonic crystals : molding the flow of light. 2nd ed. 2008, Princeton: Princeton University Press. xiv, 286 p.

16. Skorobogatiy, M. and J. Yang, Fundamentals of photonic crystal guiding. 2009, Cambridge, UK ; New York: Cambridge University Press. x, 267 p.

17. Ozbay, E., Plasmonics: merging photonics and electronics at nanoscale dimensions. Science, 2006. 311(5758): p. 189-93.

18. Gramotnev, D.K. and S.I. Bozhevolnyi, Plasmonics beyond the diffraction limit. Nature Photonics, 2010. 4(2): p. 83-91.

19. Maier, S.A. and H.A. Atwater, Plasmonics: Localization and guiding of electromagnetic energy in metal/dielectric structures. Journal of Applied Physics, 2005. 98(1).

20. Maier, S.A. and SpringerLink (Online service), Plasmonics : fundamentals and applications. 2007, New York: Springer. xxiv, 223 p.

21. Forstmann, F. and R.R. Gerhardts, METAL OPTICS NEAR THE PLASMA FREQUENCY. Festkorperprobleme-Advances in Solid State Phyics, 1982. 22: p. 291-323.

22. Hutter, E. and J.H. Fendler, Exploitation of localized surface plasmon resonance. Advanced Materials, 2004. 16(19): p. 1685-1706.

23. Hamamoto, K., et al., An original planar multireflection system for sensing using the local surface plasmon resonance of gold nanospheres. Journal of Optics a-Pure and Applied Optics, 2006. 8(3): p. 268-271.

24. Link, S. and M.A. El-Sayed, Spectral properties and relaxation dynamics of surface plasmon electronic oscillations in gold and silver nanodots and nanorods. Journal of Physical Chemistry B, 1999. 103(40): p. 8410-8426.

25. Taflove, A., Computational electrodynamics : the finite-difference time-domain method. 1995, Boston: Artech House. xvii, 599 p.

26. Grimault, A.S., A. Vial, and M.L. De La Chapelle, Modeling of regular gold nanostructures arrays for SERS applications using a 3D FDTD method. Applied Physics B-Lasers and Optics, 2006. 84(1-2): p. 111-115.

27. Dridi, M. and A. Vial, FDTD Modeling of Gold Nanoparticles in a Nematic Liquid Crystal: Quantitative and Qualitative Analysis of the Spectral Tunability. Journal of Physical Chemistry C, 2010. 114(21): p. 9541-9545.

28. Appavoo, K., et al., Spectral modulation of single plasmonic nanostructures, in Synthesis and Photonics of Nanoscale Materials Vii, J.J. Dubowski, D.B. Geohegan, and F. Trager, Editors. 2010, Spie-Int Soc Optical Engineering: Bellingham.

29. Xu, J.J., et al., Optical properties and surface-enhanced Raman scattering of quasi-3D gold plasmonic nanostructures, in Plasmonics: Metallic Nanostructures and Their Optical Properties Viii, M.I. Stockman, Editor. 2010, Spie-Int Soc Optical Engineering: Bellingham.

30. Grand, J., et al., Optical extinction Spectroscopy of oblate, prolate and ellipsoid shaped gold nanoparticles: Experiments and theory. Plasmonics, 2006. 1(2-4): p. 135-140.

31. Zhang, M.J., X.L. Zhou, and Y.Q. Fu, Plasmonic Resonance Excited Extinction Spectra of Cross-Shaped Ag Nanoparticles. Plasmonics, 2010. 5(4): p. 355-361.

32. Wang, Q. and S.T. Ho, Implementation of Perfectly Matched Layer Boundary Condition for Finite-Difference Time-Domain Simulation Truncated With Gain Medium. Journal of Lightwave Technology, 2011. 29(10): p. 1453-1459.

33. Wang, W.H., et al., Light Propagation in Curved Silver Nanowire Plasmonic Waveguides. Nano Letters, 2011. 11(4): p. 1603-1608.

34. Lau, B., M.A. Swillam, and A.S. Helmy, Hybrid orthogonal junctions: wideband plasmonic slot-silicon waveguide couplers. Optics Express, 2010. 18(26): p. 27048-27059.

35. Mock, A., First principles derivation of microcavity semiconductor laser threshold condition and its application to FDTD active cavity modeling. Journal of the Optical Society of America B-Optical Physics, 2010. 27(11): p. 2262-2272.

36. Ahmed, I., et al., Modeling and simulation of active plasmonics with the FDTD method by using solid state and Lorentz-Drude dispersive model. Journal of the Optical Society of America B-Optical Physics, 2011. 28(3): p. 352-359.

37. Kim, H.S., et al., Analysis of rectangular ring resonator sensor with photonic crystal microcavity, in Physics and Simulation of Optoelectronic Devices Xvii, M. Osinski, B. Witzigmann, and F. Henneberger, Editors. 2009, Spie-Int Soc Optical Engineering: Bellingham.

38. Shi, S.Y., et al., Modeling of light amplification and enhanced spontaneous emission in silicon nanocrystals. Journal of Nanophotonics, 2009. 3.

39. Li, J., Y.D. Yang, and Y.Z. Huang, Design of quantum cascade microcavity lasers based on Q factor versus etching depth. Journal of the Optical Society of America B-Optical Physics, 2009. 26(8): p. 1484-1491.

40. Lee, P.T., et al., High quality factor microcavity lasers realized by circular photonic crystal with isotropic photonic band gap effect. Applied Physics Letters, 2007. 90(15).

41. Fong, C.Y. and A.W. Poon, Planar corner-cut square microcavities: ray optics and FDTD analysis. Optics Express, 2004. 12(20): p. 4864-4874.

42. Lopez-Alonso, J.M., J.M. Rico-Garcia, and J. Alda, Photonic crystal characterization by FDTD and principal component analysis. Optics Express, 2004. 12(10): p. 2176-2186.

43. Yee, K.S., NUMERICAL SOLUTION OF INITIAL BOUNDARY VALUE PROBLEMS INVOLVING MAXWELLS EQUATIONS IN ISOTROPIC MEDIA. Ieee Transactions on Antennas and Propagation, 1966. AP14(3): p. 302-307.

44. Johnson, S.G. and J.D. Joannopoulos, Photonic crystals : the road from theory to practice. 2002, Boston: Kluwer Academic Publishers. 156 p.

45. Caloz, C. and T. Itoh, Electromagnetic metamaterials: transmission line theory and microwave applications: the engineering approach. 2006, Hoboken, N.J.: John Wiley & Sons. xviii, 352 p.

46. Bose, J.C., The rotation of plane of polarisation of electric waves by a twisted structure. Current Science, 1996. 70(2): p. 178-180.

47. Decker, M., et al., Circular dichroism of planar chiral magnetic metamaterials. Optics Letters, 2007. 32(7): p. 856-858.

48. Klein, M.W., et al., Second-harmonic generation from magnetic metamaterials. Science, 2006. 313(5786): p. 502-504.

49. Klein, M.W., et al., Experiments on second- and third-harmonic generation from magnetic metamaterials. Optics Express, 2007. 15(8): p. 5238-5247.

50. Fang, N., et al., Sub-diffraction-limited optical imaging with a silver superlens. Science, 2005. 308(5721): p. 534-7.

51. Landy, N.I., et al., Perfect metamaterial absorber. Phys Rev Lett, 2008. 100(20): p. 207402.

52. Cai, W.S., et al., Optical cloaking with metamaterials. Nature Photonics, 2007. 1(4): p. 224-227.

53. Smolyaninov, II, et al., Anisotropic Metamaterials Emulated by Tapered Waveguides: Application to Optical Cloaking. Physical Review Letters, 2009. 102(21).

54. Veselago, V.G., ELECTRODYNAMICS OF SUBSTANCES WITH SIMULTANEOUSLY NEGATIVE VALUES OF SIGMA AND MU. Soviet Physics Uspekhi-Ussr, 1968. 10(4): p. 509-&.

55. Depine, R.A. and A. Lakhtakia, A new condition to identify isotropic dielectric-magnetic materials displaying negative phase velocity. Microwave and Optical Technology Letters, 2004. 41(4): p. 315-316.

56. Pendry, J.B., et al., Magnetism from conductors and enhanced nonlinear phenomena. Ieee Transactions on Microwave Theory and Techniques, 1999. 47(11): p. 2075-2084.

57. Pendry, J.B., Negative refraction makes a perfect lens. Phys Rev Lett, 2000. 85(18): p. 3966-9.

58. Ishikawa, A., T. Tanaka, and S. Kawata, Frequency dependence of the magnetic response of split-ring resonators. Journal of the Optical Society of America B-Optical Physics, 2007. 24(3): p. 510-515.

59. Linden, S., et al., Magnetic response of metamaterials at 100 terahertz. Science, 2004. 306(5700): p. 1351-1353.

60. Enkrich, C., et al., Magnetic metamaterials at telecommunication and visible frequencies. Physical Review Letters, 2005. 95(20).

61. Schweizer, H., et al., Negative permeability around 630 nm in nanofabricated vertical meander metamaterials. Physica Status Solidi a-Applications and Materials Science, 2007. 204: p. 3886-3900.

62. Zhou, J., et al., Saturation of the magnetic response of split-ring resonators at optical frequencies. Physical Review Letters, 2005. 95(22).

63. Klein, M.W., et al., Single-slit split-ring resonators at optical frequencies: limits of size scaling. Optics Letters, 2006. 31: p. 1259-1261.

64. Corrigan, T.D., et al., Optical plasmonic resonances in split-ring resonator structures: an improved LC model. Opt Express, 2008. 16(24): p. 19850-64.

65. Lahiri, B., et al., Magnetic response of split ring resonators (SRRs) at visible frequencies. Optics Express, 2010. 18(3): p. 3210-3218.

66. Smith, D.R., et al., Composite medium with simultaneously negative permeability and permittivity. Phys Rev Lett, 2000. 84(18): p. 4184-7.

67. Li, Z., K. Aydin, and E. Ozbay, Determination of the effective constitutive parameters of bianisotropic metamaterials from reflection and transmission coefficients. Phys Rev E Stat Nonlin Soft Matter Phys, 2009. 79(2 Pt 2): p. 026610.

68. Smith, D.R., et al., Electromagnetic parameter retrieval from inhomogeneous metamaterials. Phys Rev E Stat Nonlin Soft Matter Phys, 2005. 71(3 Pt 2B): p. 036617.

69. Kaplan, A.F., et al., Subwavelength grating structures with magnetic resonances at visible frequencies fabricated by nanoimprint lithography for large area applications. Journal of Vacuum Science & Technology B, 2009. 27(6): p. 3175-3179.

70. Yuan, H.K., et al., A negative permeability material at red light. Optics Express, 2007. 15(3): p. 1076-1083.

71. Osawa, M., Dynamic processes in electrochemical reactions studied by surface-enhanced infrared absorption spectroscopy (SEIRAS). Bulletin of the Chemical Society of Japan, 1997. 70(12): p. 2861-2880.

72. Matsumoto, M., et al., SURFACTANT MONOLAYERS ON A CLEAN MERCURY SURFACE - APPARATUS AND EXPERIMENTS. Colloid and Polymer Science, 1990. 268(12): p. 1174-1178.

73. Maier, S.A., et al., Plasmonics - A route to nanoscale optical devices. Advanced Materials, 2001. 13(19): p. 1501-+.

74. Zhang, X.Y., et al., Ultrastable substrates for surface-enhanced Raman spectroscopy: Al2O3 overlayers fabricated by atomic layer deposition yield improved anthrax biomarker detection. Journal of the American Chemical Society, 2006. 128(31): p. 10304-10309.

75. Haes, A.J., et al., Detection of a biomarker for Alzheimer's disease from synthetic and clinical samples using a nanoscale optical biosensor. Journal of the American Chemical Society, 2005. 127(7): p. 2264-2271.

76. Homola, J., S.S. Yee, and G. Gauglitz, Surface plasmon resonance sensors: review. Sensors and Actuators B-Chemical, 1999. 54(1-2): p. 3-15.

77. Kuo, W.-K. and C.-H. Chang, Phase detection sensitivity enhancement of surface plasmon resonance sensor in a heterodyne interferometer system. Appl. Opt., 2011. 50(10): p. 1345-1349.

78. Ran, B. and S.G. Lipson, Comparison between sensitivities of phase and intensity detection in surface plasmon resonance. Optics Express, 2006. 14(12): p. 5641-5650.

79. Nelson, S.G., K.S. Johnston, and S.S. Yee, High sensitivity surface plasmon resonance sensor based on phase detection. Sensors and Actuators B-Chemical, 1996. 35(1-3): p. 187-191.

80. Yu, X.L., D.X. Wang, and Z.B. Yan, Simulation and analysis of surface plasmon resonance biosensor based on phase detection. Sensors and Actuators B-Chemical, 2003. 91(1-3): p. 285-290.

81. Yonzon, C.R., et al., Towards advanced chemical and biological nanosensors - An overview. Talanta, 2005. 67(3): p. 438-448.

82. Zhang, Z.Y. and Y.P. Zhao, Tuning the optical absorption properties of Ag nanorods by their topologic shapes: A discrete dipole approximation calculation. Applied Physics Letters, 2006. 89(2).

83. Tompkins, H.G., E.A. Irene, and Knovel (Firm), Handbook of ellipsometry. 2005, William Andrew Pub. ;Springer: Norwich, NY; Heidelberg, Germany. p. xvi, 870 p.

84. Sun, Y. and Y. Xia, Shape-controlled synthesis of gold and silver nanoparticles. Science, 2002. 298(5601): p. 2176-9.

85. Chou, S.Y., P.R. Krauss, and P.J. Renstrom, Imprint lithography with 25-nanometer resolution. Science, 1996. 272(5258): p. 85-87.

86. Guo, L.J., Nanoimprint lithography: Methods and material requirements. Advanced Materials, 2007. 19(4): p. 495-513.

87. Lucas, B.D., et al., Nanoimprint lithography based approach for the fabrication of large-area, uniformly oriented plasmonic arrays. Advanced Materials, 2008. 20(6): p. 1129-+.

88. Kronig, R.D.L., On the theory of dispersion of x-rays. Journal of the Optical Society of America and Review of Scientific Instruments, 1926. 12(6): p. 547-557.

89. McCall, S.L., et al., WHISPERING-GALLERY MODE MICRODISK LASERS. Applied Physics Letters, 1992. 60(3): p. 289-291.

90. Zhang, Z.Y., et al., Visible submicron microdisk lasers. Applied Physics Letters, 2007. 90(11).

91. Song, Q., et al., Near-IR subwavelength microdisk lasers. Applied Physics Letters, 2009. 94(6).

92. Hill, M.T., et al., Lasing in metallic- Coated nanocavities. Nature Photonics, 2007. 1(10): p. 589-594.

93. Feigenbaum, E. and M. Orenstein, Optical 3D cavity modes below the diffraction-limit using slow-wave surface-plasmon-polaritons. Optics Express, 2007. 15(5): p. 2607-2612.

94. Manolatou, C. and F. Rana, Subwavelength nanopatch cavities for semiconductor plasmon lasers. Ieee Journal of Quantum Electronics, 2008. 44(5-6): p. 435-447.

95. Mizrahi, A., et al., Low threshold gain metal coated laser nanoresonators. Optics Letters, 2008. 33(11): p. 1261-1263.

96. Min, B.K., et al., High-Q surface-plasmon-polariton whispering-gallery microcavity. Nature, 2009. 457(7228): p. 455-U3.

97. Chin, M.K., D.Y. Chu, and S.T. Ho, ESTIMATION OF THE SPONTANEOUS EMISSION FACTOR FOR MICRODISK LASERS VIA THE APPROXIMATION OF WHISPERING-GALLERY MODES. Journal of Applied Physics, 1994. 75(7): p. 3302-3307.

98. Heebner, J.E., T.C. Bond, and J.S. Kallman, Generalized formulation for performance degradations due to bending and edge scattering loss in microdisk resonators. Optics Express, 2007. 15(8): p. 4452-4473.

99. Kim, M.W., et al., Subwavelength Surface Plasmon Optical Cavity-Scaling, Amplification, and Coherence. Ieee Journal of Selected Topics in Quantum Electronics, 2009. 15(5): p. 1521-1528.

100. Barnes, W.L., A. Dereux, and T.W. Ebbesen, Surface plasmon subwavelength optics. Nature, 2003. 424(6950): p. 824-830.

101. Johnson, P.B. and R.W. Christy, OPTICAL-CONSTANTS OF NOBLE-METALS. Physical Review B, 1972. 6(12): p. 4370-4379.

102. Stegeman, G.I., R.F. Wallis, and A.A. Maradudin, Excitation of surface polaritons by end-fire coupling. Optics Letters, 1983. 8(7): p. 386-8.

103. Sarid, D., LONG-RANGE SURFACE-PLASMA WAVES ON VERY THIN METAL-FILMS. Physical Review Letters, 1981. 47(26): p. 1927-1930.

104. Amano, T., et al., Laser charaderistics of 1.3-mu m quantum dots laser with high-density quantum dots. Ieee Journal of Selected Topics in Quantum Electronics, 2007. 13(5): p. 1273-1278.

105. Egorov, A.Y., A.E. Zhukov, and V.M. Ustinov, 1.3 mu m GaAs-based quantum well and quantum dot lasers: Comparative analysis. Journal of Electronic Materials, 2001. 30(5): p. 477-481.

106. Vahala, K.J., Optical microcavities. Nature, 2003. 424(6950): p. 839-846.

107. Zhang, Y., et al., Photonic crystal nanobeam lasers. Applied Physics Letters, 2010. 97(5).

108. Pelton, M., et al., Three-dimensionally confined modes in micropost microcavities: Quality factors and Purcell factors. Ieee Journal of Quantum Electronics, 2002. 38(2): p. 170-177.

109. Srinivasan, K., M. Borselli, and O. Painter, Cavity Q, mode volume, and lasing threshold in small diameter AlGaAs microdisks with embedded quantum dots. Optics Express, 2006. 14(3): p. 1094-1105.

110. Gaspar-Armenta, J.A. and F. Villa, Band-structure properties of one-dimensional photonic crystals under the formalism of equivalent systems. Journal of the Optical Society of America B-Optical Physics, 2004. 21(2): p. 405-412.

111. Robertson, W.M. and M.S. May, Surface electromagnetic wave excitation on one-dimensional photonic band-gap arrays. Applied Physics Letters, 1999. 74(13): p. 1800-1802.

112. Yeh, P., A. Yariv, and C.S. Hong, ELECTROMAGNETIC PROPAGATION IN PERIODIC STRATIFIED MEDIA .1. GENERAL THEORY. Journal of the Optical Society of America, 1977. 67(4): p. 423-438.

113. Ponizovskaya, E.V. and A.M. Bratkovsky, Negative index materials with gain media for fast modulation. Applied Physics a-Materials Science & Processing, 2009. 95(4): p. 1137-1142.

114. Courant, R., Friedric.K, and H. Lewy, ON PARTIAL DIFFERENCE EQUATIONS OF MATHEMATICAL PHYSICS. Ibm Journal of Research and Development, 1967. 11(2): p. 215-&.

115. Sheen, D.M., et al., APPLICATION OF THE 3-DIMENSIONAL FINITE-DIFFERENCE TIME-DOMAIN METHOD TO THE ANALYSIS OF PLANAR MICROSTRIP CIRCUITS. Ieee Transactions on Microwave Theory and Techniques, 1990. 38(7): p. 849-857.

116. Monk, P. and E. Suli, A CONVERGENCE ANALYSIS OF YEE SCHEME ON NONUNIFORM GRIDS. Siam Journal on Numerical Analysis, 1994. 31(2): p. 393-412.

117. Monk, P. and E. Suli, ERROR-ESTIMATES OF YEE METHOD OF NONUNIFORM GRIDS. Ieee Transactions on Magnetics, 1994. 30(5): p. 3200-3203.

118. Rakic, A.D., et al., Optical properties of metallic films for vertical-cavity optoelectronic devices. Appl Opt, 1998. 37(22): p. 5271-83.